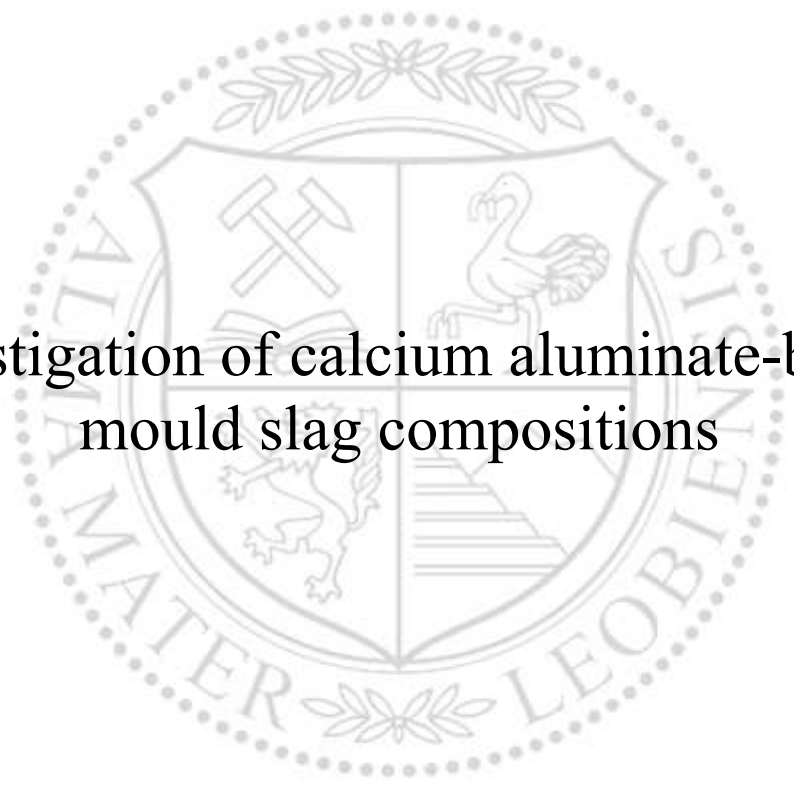




Chair of Ceramics

Master's Thesis



Investigation of calcium aluminate-based
mould slag compositions

Chongyang Chen

May 2019

AFFIDAVIT

I declare on oath that I wrote this thesis independently, did not use other than the specified sources and aids, and did not otherwise use any unauthorized aids.

I declare that I have read, understood, and complied with the guidelines of the senate of the Montanuniversität Leoben for "Good Scientific Practice".

Furthermore, I declare that the electronic and printed version of the submitted thesis are identical, both, formally and with regard to content.

Date 01.05.2019

Signature Author
Chongyang, Chen
Matriculation Number: 01600920

This thesis is dedicated to my beloved parents and girlfriend.

Acknowledgement

I would first like to thank my thesis supervisor Dipl.-Ing. Dr. mont. Irmtraud Marschall of the Chair of Ceramic at Montan University. The door to Mrs. Marschall office was always open whenever I ran into trouble or had a question about my research writing. She consistently allowed this thesis to be my own work, and guided me in the right direction whenever she thought I needed it.

I would also like to express my sincere appreciation to my supervisor O.Univ.-Prof. Dipl.-Ing. Dr. mont. Harald Harmuth. He taught me the ceramic knowledge which helped me a lot with my thesis. His serious scientific attitude and working style deeply affect and inspire me.

Besides my professor, I wish to thank various people for their contribution to this project: Mr. Christian Schober, Mr. Christian Hochenleuthner, Mr. Robert Caks, Mr. Horst Hopfinger, Dipl.-Ing. Dr. mont. Nathalie Kölbl and Mrs. Manuela Ortner.

Last but not least, I would like to thank my parents Chen Liangquan, Su Ping, and my girlfriend Wang Chen for their supporting, understanding and patience.

Abstract

The purpose of the research work was to provide a chemical composition for mould slag for casting alumina alloyed steel having a viscosity at 1300 °C lower than 0.25 Pa·s and a liquidus temperature below 1250 °C. Furthermore, SiO₂ content should not exceed 10 mass% and B₂O₃ should be avoided according to the state of the art research.

To achieve this goal, CaO-Al₂O₃ based slags with addition of SiO₂, Na₂O, Li₂O, CaF₂, MgO, K₂O, TiO₂ and SrO were investigated. FactSage was utilized to find a composition, which would satisfy the aforementioned requirements. Then, samples were prepared, heat treated at 1400 °C and quenched to room temperature by casting on a steel plate. The samples were investigated by simultaneous thermal analysis, X-ray diffraction and scanning electron and rheometer. Additional single experiments were performed using Furnace Crystallization Test, Inclined Plane Test, Single Hot Thermocouple Technique and quenching liquid slag to 900 °C.

From the results the following conclusions could be drawn. In this slag type the substitution of some CaO by SrO has a negative effect on lowering viscosity and the liquidus temperature. The viscosity increases with rising SrO content owing to the larger ion radius of Sr²⁺. The liquidus temperature increases as well. Increasing MgO content to substitute CaO increases the liquidus temperature due to the formation of an additional high melting phase which might be periclase (MgO). CaF₂ decreases the viscosity only in a limited content range. In this range larger structure units can be broken to single units, CaF₂ may work as a network modifier. Otherwise CaF₂ works as a network former generating an Al-F-Al bond by dipole – dipole interaction, which increases the viscosity. For liquidus temperature a minimum was observed at 10.95 mol% CaF₂. Finally, Li₂O is the most effective network modifier per unit weight. It could drastically decrease the viscosity due to its small ion radius, which causes low inner friction in liquidus state. Contrary to the FactSage results, rising Li₂O will decrease the liquidus temperature.

So far, the best result was achieved with composition No.21. According to the simultaneous thermal analysis the sample was totally liquid from 1236 °C on, which is satisfactory. However, its viscosity of 0.283 Pa·s at 1300 °C is too high. Increasing the Li₂O content may decrease the viscosity.

Table of contents

1 Problem definition	1
2 State of the art.....	2
2.1 Introduction.....	2
2.2 Mould slag and heat transfer.....	2
2.3 Important physical and chemical properties of mould slag	4
2.3.1 Viscosity	4
2.3.2 Liquidus, solidification and break temperature	5
2.3.3 Crystallization tendency.....	6
2.3.4 Reaction behavior between steel and slag	7
2.4 Mould slag composition	7
2.4.1 Effect of TiO_2	8
2.4.2 Effect of MgO	9
2.4.3 Effect of Li_2O	9
2.4.4 Effect of Na_2O	10
2.4.5 Effect of CaF_2	10
2.4.6 Effect of K_2O	11
3 Experimental	12
3.1 Experimental methodology.....	12
3.2 Sample Preparation	13
3.3 FactSage	14
3.4 Viscosity measurement.....	14
3.5 Differential thermal analysis	16
3.6 Furnace crystallization test.....	17
3.7 X-ray diffraction analysis	17
3.8 Scanning electron microscopy (SEM) analysis.....	18
3.9 Single hot thermocouple technique	20
3.10 Inclined plane test.....	21
4 Result and discussion.....	22
4.1 Effect of substituting CaO with SrO	22
4.1.1 Glass formation of mould slag during quenching	22
4.1.2 Effect on viscosity and break temperature	24
4.2 Effect of using MgO to substitute CaO	27

4.2.1 Glass formation of mould slag during quenching	27
4.2.2 Effect on liquidus temperature	29
4.3 Effect of CaF ₂	30
4.3.1 Glass formation of mould slag during quenching	30
4.3.2 Effect on mass loss	32
4.3.4 Effect on the viscosity	35
4.3.5 Phase formation	36
4.4 Effect of Li ₂ O	37
4.4.1 Glass formation of mould slag during quenching	37
4.4.2 Effect on viscosity and break temperature	39
4.4.3 Inclined plane test to estimate the viscosity	41
4.4.4 Effect on liquidus temperature and crystallization temperature	41
4.4.5 Single hot thermocouple technique (SHTT) to analyze the crystallization behavior	43
4.4.6 High temperature quenching from 1400 °C to 900 °C	44
5 Conclusion	51
Reference	52
Appendix	I

1 Problem definition

In the continuous casting process of steel, mould slag performance is a key factor to good steel quality. An important engineering challenge is associated with the casting of TRIP (transformation induced plasticity) steels, which frequently contains considerable amount of Al. For conventional mould slag composition, on one hand, SiO_2 reacts with the Al of the steel to form Al_2O_3 and alters both the steel and slag properties. The liquidus temperature and the viscosity of the slag may increase due to the flux of Al_2O_3 , which could cause problems such as low lubrication. Therefore, it is necessary to reduce the SiO_2 content. On the other hand, with Al decreasing in steel, the liquidus temperature of steel is decreased. Low steel temperature will lead to lower vertical heat transfer, which results in lower melting rate of slag and lower slag pools. In order to cast high-Al alloyed steel, it is necessary to find a slag with a low melting point, since the steel provides less thermal transfer to melt the mould slag during continuous casting.

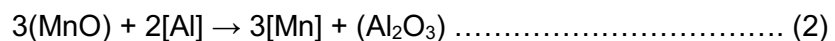
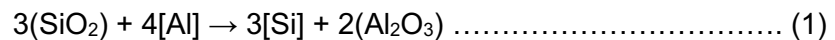
Current state of the art research applies a common strategy to increase the Al_2O_3 content by using calcium aluminates based mould slag with the addition of less reducible fluxes (e.g. Na_2O , Li_2O , K_2O , CaF_2). However, problems still exist when using the mentioned approach, such as the high price of Li_2O , environmental pollution caused by CaF_2 , and the low lubrication.

The purpose of the research is to provide a chemical composition for mould slag composition having a viscosity at 1300 °C lower than 0.25 Pa·s and a liquidus temperature below 1250 °C. Furthermore, SiO_2 should be significantly decreased and B_2O_3 should be avoided according to the state of the art research.

2 State of the art

2.1 Introduction

Recently, owing to the development of automobile and electric industry, TRIP steel application has enjoyed a great deal of industrial expansion. There are lots of advantages of using TRIP steel compared with normal steel. For example, TRIP steel has better strength per unit weight, corrosion resistance, thermal conductivity, and electrical conductivity. However, as shown in Eqs. (1) and (2), during continuous casting, a redox reaction between Al and both SiO₂ and MnO may occur. This may increase the viscosity, the melting temperature, and alters phase formation of the mould slag. This leads to unsatisfying lubrication and heat transfer [1]. A bad performance of the mould slag could result in poor surface quality of the cast slabs.



To prevent the pickup of Al by the slag, the amount of SiO₂ and MnO must be as low as possible. Researchers have focused on lime-alumina based mould slags in order to replace conventional siliceous slags [2-5].

2.2 Mould slag and heat transfer

The mould slag has five main functions in continuous casting [6]:

- 1) Protection of the meniscus of the steel from oxidation.
- 2) Thermal insulation.
- 3) Absorption of inclusions.
- 4) Control of the heat transfer.
- 5) Lubrication of the strand.

As shown in Figure 1, the mould powder, which is in contact with the liquid steel, becomes liquidus due to the heat from the steel. Then the liquid slag infiltrates into the gap between the mould and the shell. The slag film is formed, which contains three layers: liquidus slag layer, glassy slag layer and crystalline slag layer. These layers with satisfactory thermal resistance ensure the formation of the steel shell. Controlling mould heat transfer rate is one of the most important functions of mould slag [7].

Figure 2 depicts the heat transfer from the boundary of solidifying shell to the copper mould [8]. The position and temperature are represented as the horizontal and vertical axis, respectively. T_{Mold} is the temperature of copper mould. T_{MC} is the temperature of

the boundary of solid film, which is near the copper mould. T_{CL} is the temperature of the surface between solid film and liquidus film. T_{LS} is the temperature of the surface between liquidus film and solidifying shell. T_{Sol} is the temperature of the steel. Some researchers propose that the slag heat transfer rate would be reduced when the crystallinity is increased in slag film [9-11]. Moreover, with a thicker crystalline layer, the liquidus layer gets thinner, which means the mould slag will provide poorer lubrication [8].

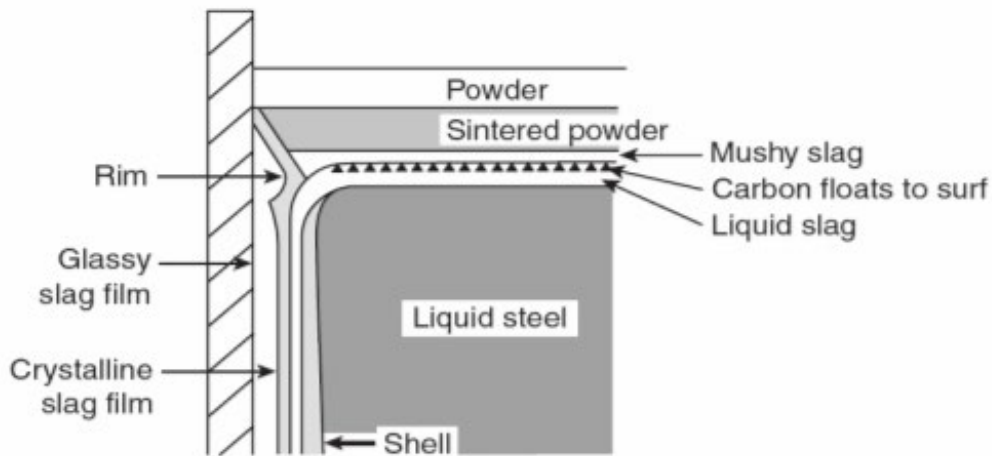


Figure 1: Schematic diagram of mould in continuous casting [12]

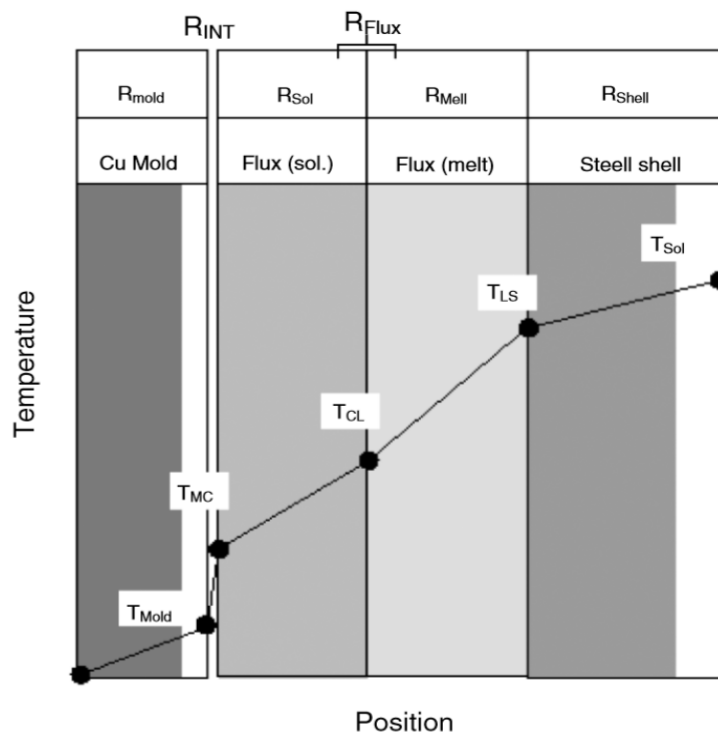


Figure 2: Heat transfer in slag film [6]

2.3 Important physical and chemical properties of mould slag

2.3.1 Viscosity

Viscosity is an important property of mold slag. It strongly affects the consumption of slag, absorption of inclusions, and corrosion of submerged nozzle [13]. The viscosity of the slag should be optimized, so that lubrication at the surface between solidified film and shell can prevent the formation of the defects in the mould. Viscosity is sensitive to the slag structure, and alteration of the chemical composition could change the slag structure [14].

To better understand how the slag structure affects the viscosity, classification of non-oxygen ions in oxides with respect to their role in the glass network is important.

Table 1: Classification of elements with respect to their role in the glass network[15]

Element	Valency Z	Ionic radius r (at KZ = 6) [pm]	Main coordination number	Interionic distance of oxides [pm]	Field strength relative to O ²⁻ -ions Z/a ²	Role in the glass network
K	1	133	8	277	0,13	Network modifier Z/a ² ≈ 0,1 ... 0,4
Na	1	98	6	230	0,19	
Li	1	78	6	210	0,23	
Ba	2	143	8	286	0,24	
Pb	2	132	8	274	0,27	
Sr	2	127	8	269	0,28	
Ca	2	106	8	248	0,33	
Mn	2	91	6	223	0,40	
Fe	2	83	6	215	0,43	
Mn	2	83	4	203	0,49	Intermediate oxides Z/a ² ≈ 0,5 ... 1,0
Mg	2	78	6	210	0,45	
			4	196	0,53	
Zr	4	87	8	228	0,77	
Be	2	34	4	153	0,86	
Fe	3	67	6	199	0,76	
			4	188	0,85	
Al	3	57	6	189	0,84	Network former Z/a ² ≈ 1,4 ... 2,0
			4	177	0,96	
Ti	4	64	6	196	1,04	
B	3	20	4	150	1,34	
Ge	4	44	4	166	1,45	
Si	4	39	4	160	1,57	
P	5	34	4	155	2,1	

Table 1 shows the element's physical properties and its role in glass network. Dietzal's field strength for Network modifier is between 0.1 and 0.4. For Network former, the Dietzal's field strength of oxides are between 1.4 and 2.0. Dietzel's field strength for intermediate oxides is larger than those of network modifiers and lower than that of network formers, which is 0.5-1.0. Generally, the network modifier breaks the Si-O-Si and decreases the viscosity of slag. Contrary to network modifier, network former enhances the glass network which could increase the viscosity. And the intermediate oxides play different roles on network depending on the slag composition. Al₂O₃ act as network former in CaO-Al₂O₃ based slag as the substitute of SiO₂ [15].

The temperature dependence of the viscosity is frequently represented by Arrhenius equation Eqs. (3):

$$\ln \eta = \ln A + \frac{E}{RT} \dots\dots\dots (3)$$

where η is the viscosity (dPas); A is pre-exponential factor (dPas); E is the activation energy (J/mol); R is ideal gas constant, 8.134 J/(mol·K); T is the absolute temperature (K) [14]. However, the activation energy is not constant for the whole temperature range. The more accurate three-parameter equation for viscosity (η) is the Vogel-Fulcher-Tammann (VFT-equation) Eqs.(4) [16]:

$$\log \eta = A + \frac{B}{T-T_0} \dots\dots\dots (4)$$

where A, B and T_0 are constant, T is absolute temperature. Both equations show that the viscosity decrease with increasing absolute temperature.

2.3.2 Liquidus, solidification and break temperature

The liquidus temperature is the temperature when the mould slag totally melts. It is estimated by DTA. By knowing that the liquidus temperature is not above a criterion, which is important for continuous casting, it ensures that a liquidus film exists between the copper mould and steel shell [6].

The solidification temperature is defined during cooling. It is the temperature at which the first solid phase forms. It can be determined by DTA and SHTT.

The break temperature (T_{br}) is defined as a temperature at which the viscosity suddenly increases during cooling as shown in Figure 3. It is affected by the cooling rate. Break temperature is a significant property since it determines the thickness of solid and liquidus layers, which influence the heat transfer, lubrication and powder consumption properties [6].

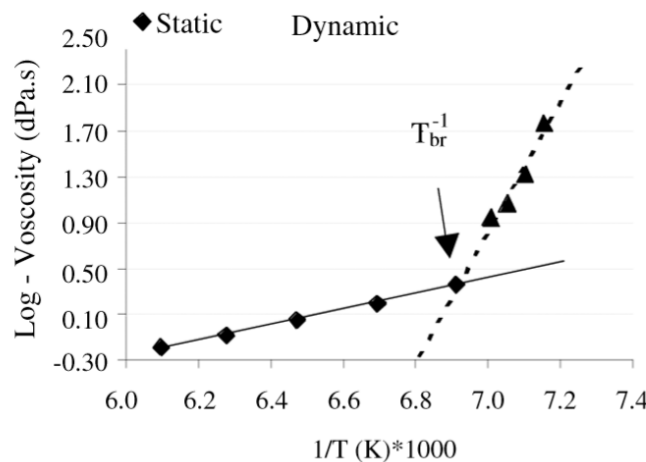


Figure 3: Temperature and viscosity curve[6]

Yu et al. [5] found that the liquidus temperature of slag increases with increasing $\text{Al}_2\text{O}_3/\text{SiO}_2$ ratio. Figure 4 shows the $\text{CaO}-\text{Al}_2\text{O}_3-\text{SiO}_2$ phase diagram. For $\text{CaO}-\text{Al}_2\text{O}_3$ based mould slag, the SiO_2 content should be as little as possible owing to the reaction with Al from steel. So, the composition could be located in the lower part of this diagram. The red circle marks the region of optimal composition due to the liquidus temperature of slag should be around $1200\text{ }^\circ\text{C}$. Although the eutectic temperatures in this area are higher than $1200\text{ }^\circ\text{C}$, there are some options to decrease the melting points by addition of other oxides and finding the optimal CaO/SiO_2 and $\text{Al}_2\text{O}_3/\text{SiO}_2$ ratios.

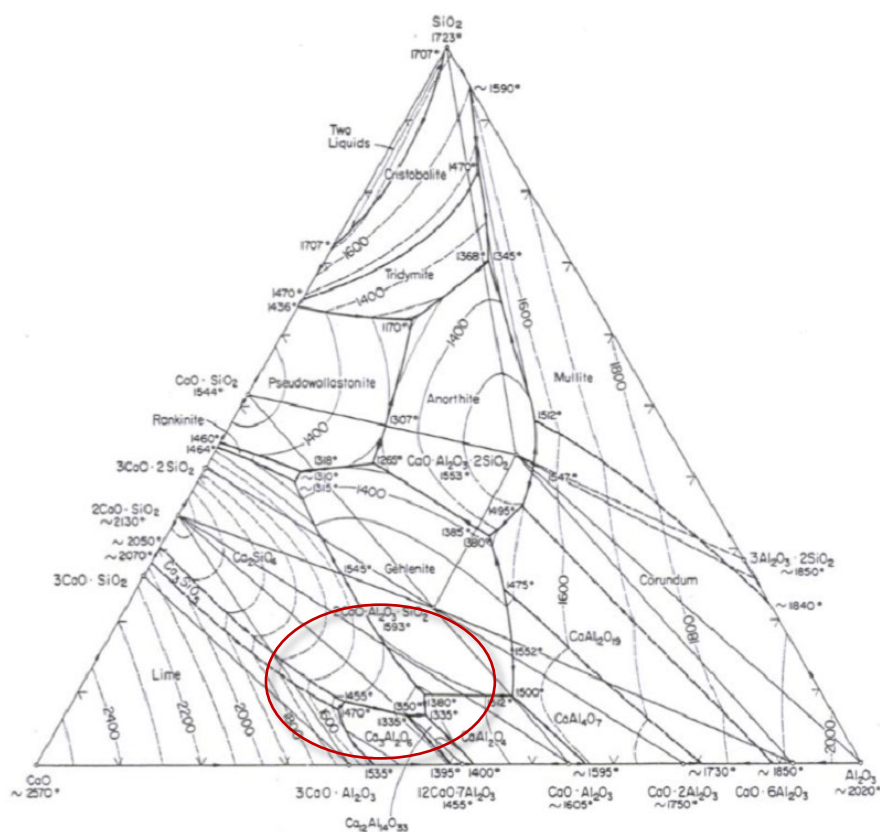


Figure 4: $\text{CaO}-\text{Al}_2\text{O}_3-\text{SiO}_2$ phase diagram (mass%, $^\circ\text{C}$) [17]

2.3.3 Crystallization tendency

The formation of crystals during continuous casting would increase the thermal resistance. The occurrence of only crystalline film will be problematic, and will lead to poor lubrication between copper mould and steel shell, which will cause defects on the steel surface [1]. Single hot thermocouple technique is applied to analyze the crystallization behavior. Hereby the time is determined for when crystallized volume reaches a certain fraction of the slag being quenched to a fixed temperature. The

amount of crystallization can be determined by analyzing the SHTT pictures. From the results a Time-Temperature-Transformation (T-T-T) curve can be drawn. [18].

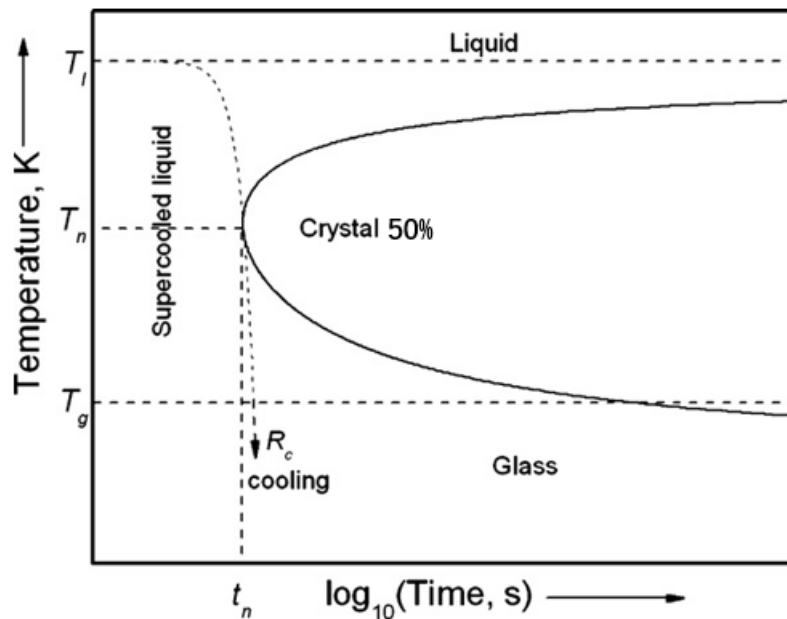


Figure 5: Typical T-T-T diagram [18]

Figure 5 displays a typical example of T-T-T diagram. At a certain temperature T_n , it takes time t_n to reach 50% crystalline fraction. And even at a very low temperature (T_g) the crystalline phase can reach 50% crystalline fraction with a longer period.

2.3.4 Reaction behavior between steel and slag

Reaction between mould slag and TRIP steel is relatively strong. In section 2.1 it was discussed that SiO_2 can react with $[\text{Al}]$ in steel. However, some other oxides, such as B_2O_3 , MnO , FeO and TiO_2 , also react with $[\text{Al}]$ during continuous casting. Usually mould slag picks up 4-5% Al_2O_3 of which about half comes from steel making processes and half from the reaction shown in Eqs. (1) and Eqs. (2) [19]. The Al pickup oxidizes to Al_2O_3 and will stay in the slag film. The reaction results in changing properties of the slag such as liquidus temperature, viscosity and lead to a larger fluctuation of the heat flux in the mould [1, 20, 21].

2.4 Mould slag composition

The common industrial mould slag for TRIP steel consists of CaO-SiO_2 based mould slag. SiO_2 is partly replaced by Al_2O_3 for the purpose of inhibiting the reaction between slag and steel [22]. The selection of an optimum CaO/SiO_2 and $\text{Al}_2\text{O}_3/\text{SiO}_2$ ratio with

respect to glass forming and liquid temperature are essential [23-25]. Fluxing agents (Na_2O , Li_2O , CaF_2 , MgO , K_2O , TiO_2) are added due to their effects on the slag properties such as lowering liquidus temperature and viscosity [7]. Some researchers suggest the addition of agents such as B_2O_3 and MnO , since their ability of reacting with steel is weaker than SiO_2 [26].

Furthermore, the amount of SiO_2 , Al_2O_3 and CaO are significant for glass forming behavior. Glassy slag promotes the lubrication behavior and can reasonably increase the thermal conductivity during casting. Figure 6 shows the glassy forming compositions in the $\text{CaO-Al}_2\text{O}_3\text{-SiO}_2$ system, the formation of glasses is obtained within the white zone by using classic quenching method [27]. Since SiO_2 content should be low, the target composition point must locate in the lower part of the triangle.

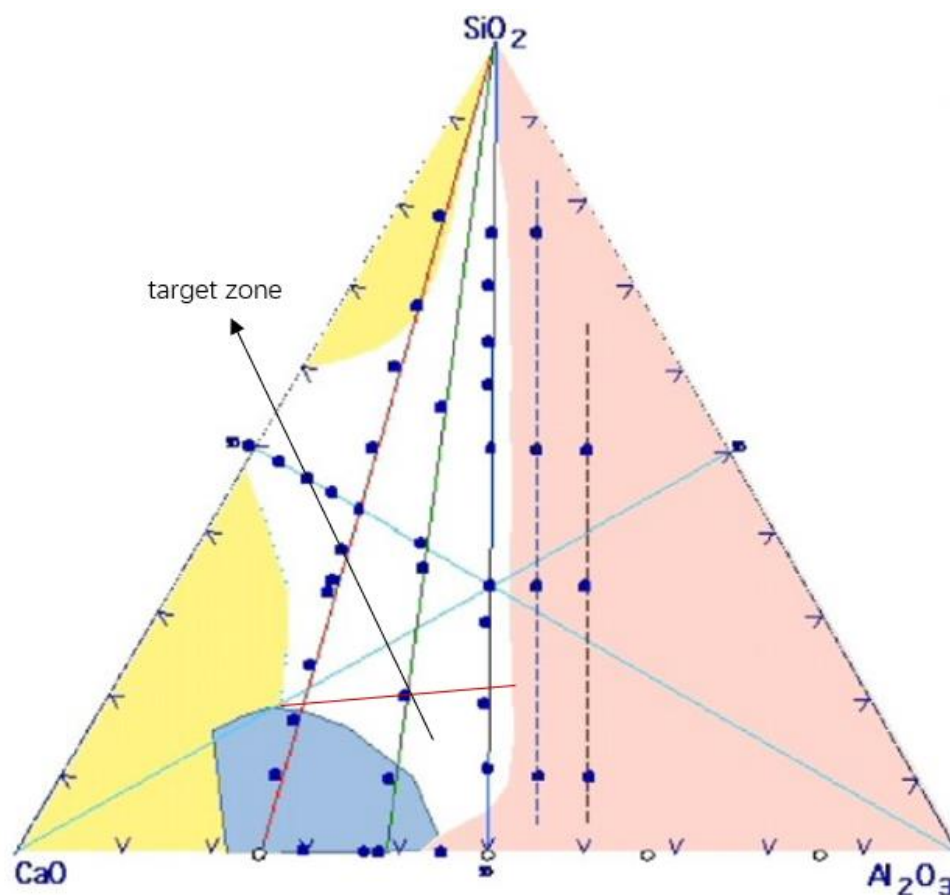


Figure 6: Glassy forming behavior in $\text{SiO}_2\text{-CaO-Al}_2\text{O}_3$ system (mol%) [27]

2.4.1 Effect of TiO_2

For $\text{CaO-Al}_2\text{O}_3$ based mould slag, TiO_2 reduces the reaction between mould flux and steel by substituting SiO_2 with TiO_2 . This is because both act as network former, and

TiO₂ is more stable than SiO₂. However, the liquidus temperature of the slag could increase with increasing TiO₂ content. The undercooling value for the start of perovskite (CaTiO₃) crystallization decreases along with increasing TiO₂ content, which means that the crystallization of CaTiO₃ is enhanced with increasing TiO₂ content [28].

2.4.2 Effect of MgO

Slag basicity is very high in CaO-Al₂O₃ based mould slag, which enhances the crystallization capability and causes poor lubrication. Therefore, MgO is introduced to retard the crystallization behavior and enhance the lubrication performance. When the MgO content is high, it tends to reduce the viscosity of the mould slag. Because MgO can release O²⁻ ions to depolymerize the network owing to its weak charge compensation effect [29]. Some researchers have pointed out that MgO can decrease the melting point of slag [7]. But it cannot replace CaO totally owing to the high eutectic temperature shown in Figure 7.

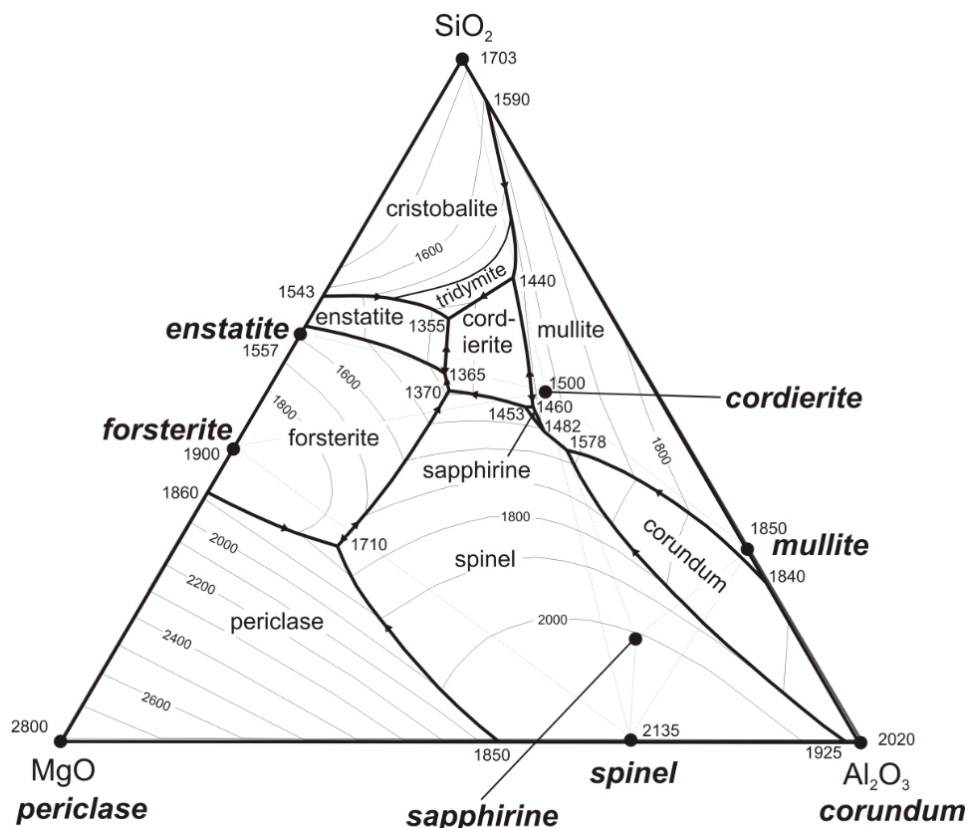


Figure 7: MgO-SiO₂-Al₂O₃ phase diagram (wt%, °C) [30]

2.4.3 Effect of Li₂O

According to Dietzal's field strength, Li₂O acts as network modifiers in glass network, which could significantly decrease the viscosity of the mould slag. Kim et al. carried out experiments that showed the reduction of viscosity with up to 2 wt% Li₂O.

Excessive Li_2O content has little impact on viscosity [31]. On the other hand, Li_2O retards the crystallization by decreasing the initial crystallization temperature and critical cooling rate [32]. Li_2O also plays an important role of inhibiting crystallization in the high-temperature region by raising the incubation time [32]. In the lower temperature region, owing to the formation of LiAlO_2 , the slag shows the highest crystallization tendency. Moreover, in fluorine containing mould slags, the addition of Li_2O could inhibit the formation of $\text{Ca}_4\text{Si}_2\text{O}_7\text{F}_2$ and $\text{Ca}_2\text{Al}_2\text{SiO}_7$ [33]. Henceforth, finding a favorable Li_2O content is important.

2.4.4 Effect of Na_2O

Increasing the Na_2O content could decrease the viscosity of the slag, because Na_2O act as a network modifier, which breaks the glass network [15]. Wang et al. suggested that Na_2O could restrain the crystallization of $\text{CaO-Al}_2\text{O}_3$ based mould slag. It reduces the crystallization temperature, but it has no effect on the critical cooling rate. And when Na_2O exceeds 10wt%, the influence on crystallization temperature becomes weak. The reason might be charge-compensation of $[\text{AlO}_4]^{5-}$ by Na^+ and thereby a stably formed structure which cannot be depolymerized easily [22].

2.4.5 Effect of CaF_2

The effect of CaF_2 on mould slag depends on the slag composition. Tsunawaki et al. [34] investigated the behavior of CaF_2 in the acidic melts. Fluorine acts as network modifier to coordinate with Si^{4+} and depolymerize the network structure, which results in the reduction of viscosity. However, when CaF_2 is added to basic melts, fluorine is present as F^- and combines with Ca^{2+} , which would not break the Si-O bonds. Gao et al. indicated that F^- ions exist in three different structure types: bond with Si^{4+} , bond with Al^{3+} and unincorporated F^- . In network structure, the molar fraction of $[\text{AlO}_4]$ -tetrahedra could decrease due to the breakage of Al-O bond by F^- ions, then F^- combines with Al^{3+} to form AlF_4^- . Also, the bonds between Si^{4+} and Si-O^0 are broken by F^- ions, and F^- bonds with Si^{4+} to form simple tetrahedral units $[\text{SiO}_n\text{F}_{4-n}]$ -tetrahedra [35]. Moreover, CaF_2 is a key component for common mould slag due to its beneficial effects to lubrication, by decreasing both the viscosity and break temperature [34]. Also, CaF_2 could form cuspidine, which decreases the heat transfer of slag. However, while the temperature is above 900°C , oxides in the slag could react with CaF_2 , resulting in gaseous fluoride emissions, which is harmful to the environment and humans' health [36]. Therefore, it is necessary to reduce the CaF_2 content as much as possible. It is not difficult to keep the lubrication behavior by using some other oxides such as Na_2O ,

Li_2O and K_2O . However, it is more difficult to figure out a suitable phase to replace cuspidine to control the horizontal heat flux [19].

2.4.6 Effect of K_2O

K_2O act as network modifier. Its effect on viscosity depends on the $\text{K}_2\text{O}/\text{Al}_2\text{O}_3$ molar ratio. HIGO et al. [37] indicated that slag viscosity increases with increasing K_2O content for $\text{K}_2\text{O}/\text{Al}_2\text{O}_3$ molar ratio <0.7 . It means the bond strength enhances with the addition of K_2O . The reason is that K^+ ions replace Ca^{2+} ions owing to the charge balancing responsibility. For the $\text{K}_2\text{O}/\text{Al}_2\text{O}_3$ molar ratio >0.9 , the viscosity will decrease with increasing K_2O . This behavior is owing to the growing amount of NBOs outpacing the average bond strength of the NBOs.

3 Experimental

3.1 Experimental methodology

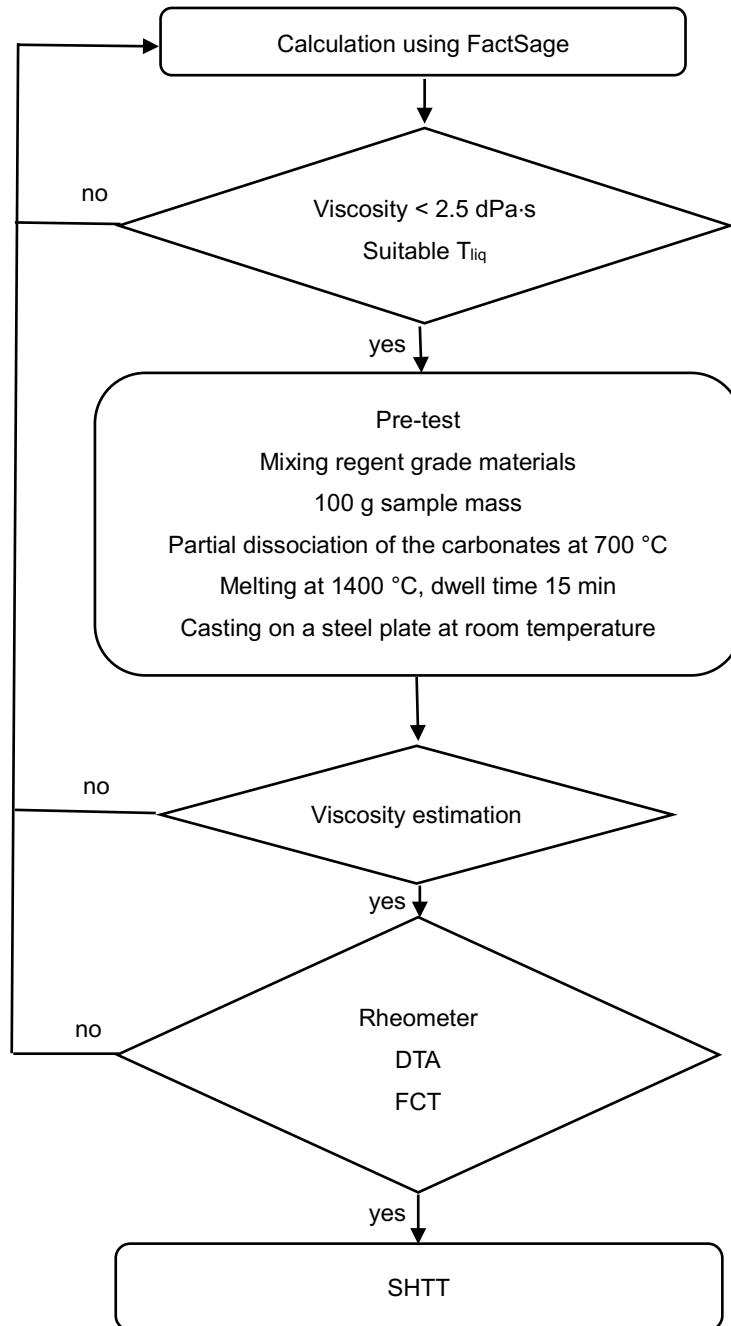


Figure 8: The flowsheet of the experiments

Figure 8 shows the flowsheet of the experimental design. First, Factsage was used to calculate a suitable composition of the slag. Unfortunately, no compositions could achieve having a liquidus temperature below 1250 °C, but pretests showed that at least

the tested composition were liquidus at 1400 °C. Next, sufficient samples were prepared for further analysis. Then, DTA (Differential thermal analysis), FCT (Furnace crystallization test) and rheometer were used to investigate the liquidus temperature, crystallization behavior and viscosity. If the sample's properties fulfilled the requirements, SHTT (Single hot thermocouple technique) was applied to analyze the crystallization behavior in more detail.

3.2 Sample Preparation

Based on on the discussion in section 2.4, nine mould fluxes were designed in the CaO-Al₂O₃-SiO₂-Na₂O-Li₂O-CaF₂-MgO-K₂O-TiO₂ system. The mixtures were made of reagent grade raw materials with a purity higher than 99%. CaCO₃, NaCO₃, Li₂CO₃, K₂CO₃ and SrCO₃ were used as raw materials to substitute CaO, Na₂O, Li₂O, K₂O and SrO owing to their stability in air. The chemical compositions are given in Table 2. It is better to analyze the chemical composition in moles due to the glass network theory. In order to analyze the properties of mould slag, the samples needed to be quenched first. The mixed powders were put into a platinum crucible, melted at 1400°C for 15 mins, and quenched on a steel plate for fast cooling.

Mixes No.11-No.16 were tested to analyze the effect of the interchange of SrO and CaO content on mould slag properties. Mixes No.16 and No.20 were tested to analyze the effect of using MgO to substitute same moles CaO. Mixes No.16, No.21, No.22 and No.23 were tested to analyze the effect of increasing CaF₂ content on mould slag properties, and mixes No.21, No.24, No.25, No.26 were tested to analyze the effect of decreasing LiO₂ content on mould slag properties.

Table 2: Chemical composition of all investigated samples [mol%]

Samples	SiO ₂	Al ₂ O ₃	CaO	Na ₂ O	Li ₂ O	CaF ₂	SrO	MgO	K ₂ O	TiO ₂
No.11	8.45	20.97	35.44	11.84	5.63	6.50	1.75	2.91	1.55	4.95
No.12	8.45	20.97	33.44	11.84	5.63	6.50	3.75	2.91	1.55	4.96
No.13	8.45	20.97	31.44	11.84	5.63	6.50	5.75	2.91	1.55	4.96
No.14	8.45	20.97	29.44	11.84	5.63	6.50	7.75	2.91	1.55	4.96
No.15	8.45	20.97	27.44	11.84	5.63	6.50	9.75	2.91	1.55	4.96
No.16	8.45	20.97	37.15	11.84	5.63	6.50	0.00	2.91	1.55	5.00
No.17	8.45	16.97	36.15	4.00	5.00	8.50	0.00	2.91	8.02	10.00
No.18	8.45	16.97	36.15	4.00	4.00	8.50	0.00	2.91	9.02	10.00
No.19	10.01	18.92	25.35	9.00	5.63	15.00	0.00	9.54	1.55	5.00
No.20	8.45	20.97	32.15	11.84	5.63	6.50	0.00	7.91	1.55	5.00
No.21	8.05	19.97	35.38	11.28	5.36	10.95	0.00	2.77	1.48	4.76
No.22	7.68	19.06	33.77	10.76	5.12	15.00	0.00	2.65	1.41	4.55
No.23	7.23	17.94	31.79	10.13	4.82	20.00	0.00	2.49	1.33	4.28
No.24	8.18	20.29	35.94	11.46	3.86	11.13	0.00	2.82	1.50	4.84
No.25	8.30	20.60	36.50	11.63	2.36	11.30	0.00	2.86	1.52	4.91
No.26	8.43	20.92	37.06	11.81	0.86	11.47	0.00	2.90	1.55	4.99

3.3 FactSage

Factsage is one of the largest database computing systems in chemical thermodynamics in the world [38]. The mould slag compositions were evaluated with FactSage, so that the liquidus temperature and viscosity at 1300 °C should be in a reasonable range.

3.4 Viscosity measurement

As shown in Figure 9, the furnace rheometer systems FRS 1800 from Anton Paar consist of a lab furnace and the rheometer head, which features the established EC

motor and air-bearing technology of the rheometer series. To protect the equipment, an air-cooled and water-cooled systems were used.

The principle of rotational viscometers is that the torque required to rotate an object in a liquid is proportional to viscosity of that liquid. By measuring the torque required to rotate the bob in a melt at a given speed, the viscosity of the sample at the known temperature can be calculated as shown in Eqs. (5).

$$\eta = \frac{\tau}{\dot{\gamma}} \text{ [Pa}\cdot\text{s]} \dots\dots\dots (5)$$

τ : Shear stress [Pa]

$\dot{\gamma}$: Shear rate [s^{-1}]

The quenched sample were ground to powder form for viscosity measurement. 35 g of the powder were filled into a platinum crucible. The bob was fixed, and the crucible was placed on the sample holder. The sample was heated up within 140 min to 1400 °C, then the bob was immersed into the liquid sample, and the rotation was started with the shear rate of 20 s^{-1} . After a dwell of 5 min the slag was cooled with 5 °C/min until a maximum torque was reached. From the measurement the viscosity depending on the temperature can be derived.



Figure 9: Viscosity measurement equipment

3.5 Differential thermal analysis

Differential thermal analysis is an analytic technique for material phase change. Some important characteristics of the mould slag, such as liquidus temperature, crystallization temperature and glass transition temperature can be measured by DTA. The amount of evaporation of mould slag also can be known by combining thermal gravimetry. The measurement was performed with a STA F3 Jupiter from Netzsch. Its cross section is given in Figure 10. Contrary to the figure, the DTA sample holder was used. The pre-melted sample was heated up with 20 °C /min until 1450 °C. Then cooled with 10 °C/min to room temperature. Ar gas purging is used as the protection gas with 70 ml/min. Temperature difference between sample and reference was analyzed. Exothermic or endothermic events of the sample were detected relative to the inert reference. Thus, the transformations data was read on the DTA curve. The peaks on the curve were enthalpy changes and were not affected by heat capacity of the sample.

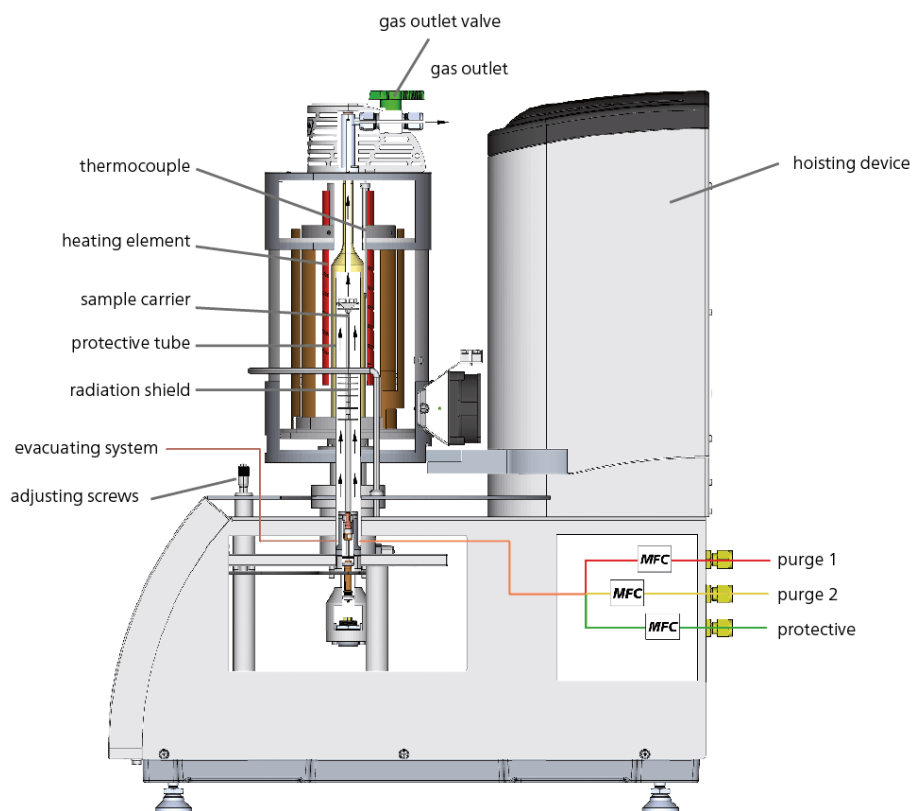


Figure 10: Differential thermal analysis equipment [39]

3.6 Furnace crystallization test

Furnace crystallization test measurement is similar to DTA measurement, but on a bigger scale. 27g of the quenched sample powder and the same mass of alumina that acts as reference material were added into separate platinum crucible. The samples were heated up within a furnace chamber to 1350 °C for a dwell time of 15 min, then cooled to room temperature with a cooling rate of 10 °C/min. There are two wires embedded in the sample and the reference to record their respective temperatures. Similar to the DTA, the calculated temperature difference refers to endothermal or exothermal events. After the FCT measurement, the solidified sample was cut into two halves, with one made into a polished section for further analysis.

3.7 X-ray diffraction analysis

X-ray powder diffraction is an efficient analysis method mainly applied for phase identification of a crystalline material and providing information in unit cell dimensions [40]. For the investigation of the phase composition, equipment Bruker D8 with fixed divergence slit and high-speed detector and a copper target was used. An X-ray beam of defined wavelength was focused on the sample. Thereby the beam was scattered at all scattering centers. The scattering centers are located on lattice planes. The beam scattered at different lattice planes must be scattered coherently to give a maximum of scattered intensity. Bragg's Law as shown in Eqs. (6) measures peak positions that can be allocated to distinctive d-spacing:

$$n \cdot \lambda = 2 \cdot d \cdot \sin(\theta) \dots\dots\dots (6)$$

where d is the spacing between the planes in the atomic lattice; λ is the wavelength; θ is the angle between incident beam and lattice planes; n is an integer [41].

As shown in Figure 11 and 12, the ground powder was added on the stage and fixed into the equipment. Evaluation of the result was done manually by comparing with standard of ICCD PDF 4 database.



Figure 11: Filled sample containers

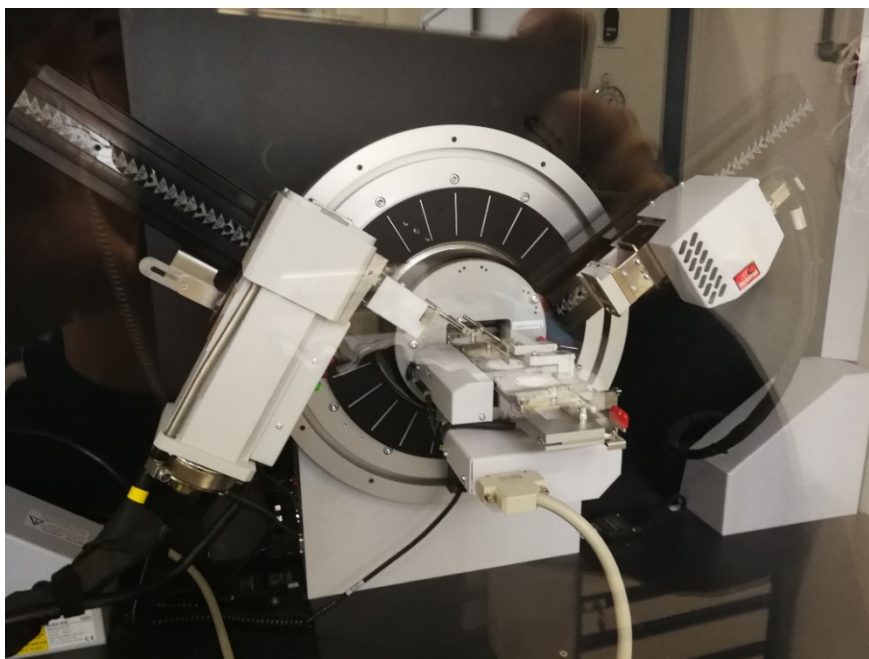


Figure 12: X-ray diffraction analysis equipment

3.8 Scanning electron microscopy (SEM) analysis

A focused beam of electrons is utilized in scanning electron microscopy to produce a diversity of signals on the surface of polished samples. The signals that are derived from electron-sample interactions may disclose information about the sample [42], including external morphology and crystalline structure.

To analyze the sample structure after crystallization, polished sections were prepared from the FCT samples. The high temperature quenched samples were investigated by a reflection microscope AX70 Olympus (Figure 14). From this an overview of the sample followed. For detailed analysis an SEM MA15 EVO (Figure 15), including an energy dispersive X-ray spectroscopy from Oxford was used.



Figure 13: Polished sample



Figure 14: Optical microscope

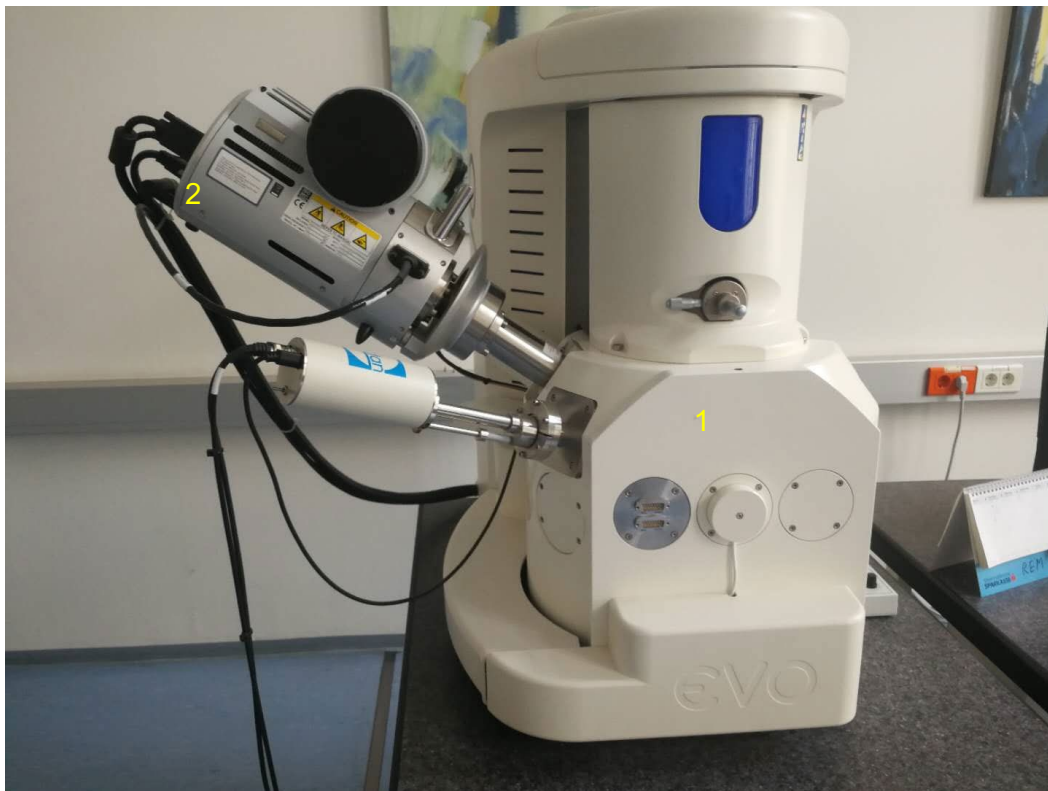


Figure 15: Scanning electron microscope (1) including energy dispersive X-ray spectroscopy detector (2).

3.9 Single hot thermocouple technique

Single hot thermocouple technique (SHTT) (Figure 17) was applied for analyzing the crystallization behaviors of mould slag.

The quenched powders were pressed together to form disc shaped sample. A tiny part of the it was put on the platinum wire which had been heated up to 1400 °C to get a melted sample, as shown in Figure 16 [33]. A stretching device was used to stretch the liquid sample to form a thin slag layer. Then the temperature of the wire was adjusted by the controller to a fixed temperature. While the melted sample transformed to glass and crystals, pictures were taken by a camera at time intervals until 95% of the sample was crystallized. By analyzing the pictures, the crystallization behavior can be quantified.

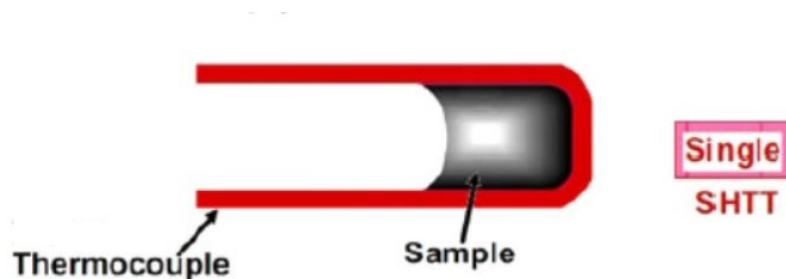


Figure 16: The schematic of single hot thermocouples [33]



Figure 17: Single hot thermocouple technique equipment

3.10 Inclined plane test

Inclined plane test is an efficient and reliable technique for characterizing the viscous behavior of the slag. As shown in Figure 18, a stainless-steel planet and a heating furnace was used. 15 g of the quenched powders were added into a platinum crucible and kept in a furnace at 1480 °C for 15 min, then the molten sample was taken out from the furnace and was poured immediately on the top of the plane, which had a 14° angle with the level table. The molten sample flowed down the plane until it solidified. Thus, a slag ribbon was formed, of which the length is proportional to the viscosity of the mould slag. Each sample was tested at least 5 times to reduce standard deviation of the mean value.

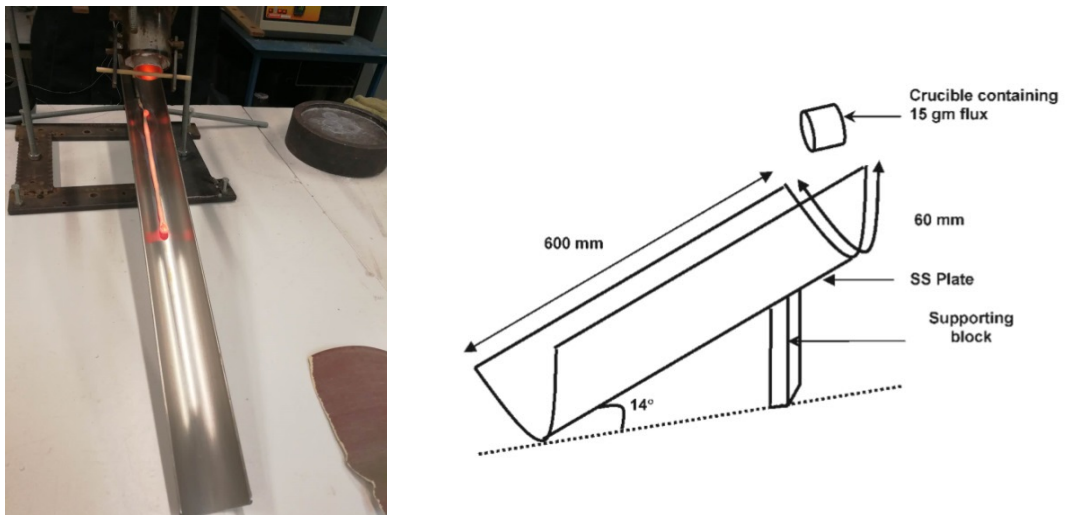


Figure 18: Inclined plane test [43]

4 Result and discussion

4.1 Effect of substituting CaO with SrO

4.1.1 Glass formation of mould slag during quenching

As shown in Table 3, the compositions of sample No.11 to No.16 gradually replace CaO with SrO mole for mole. The glassy phase formation ability can be visually assessed by quenching method. The quenched examples of sample No.11 to No.16 are shown in Figure 19, where it can be clearly observed that with the increase of SrO content, the crystal fraction increases. The XRD results of quenched samples are shown in Figure 20, which shows that the glass fraction decreases with increasing SrO content. Sodium calcium fluorite silicate ($\text{NaCa}_2\text{SiO}_4\text{F}$) and lithium aluminate (LiAlO_2) formed during quenching.

Table 3: Chemical composition of sample No.11 to No.16 [mole%]

Samples	SiO ₂	Al ₂ O ₃	CaO	Na ₂ O	Li ₂ O	CaF ₂	SrO	MgO	K ₂ O	TiO ₂	Factsage viscosity [Pa·s]	Factsage liquidus T [°C]
No.16	8.45	20.97	37.15	11.84	5.63	6.5	0	2.91	1.55	5	0.21	1443
No.11	8.45	20.97	35.44	11.84	5.63	6.5	1.75	2.91	1.55	4.95	-	-
No.12	8.45	20.97	33.44	11.84	5.63	6.5	3.75	2.91	1.55	4.96	-	-
No.13	8.45	20.97	31.44	11.84	5.63	6.5	5.75	2.91	1.55	4.96	-	-
No.14	8.45	20.97	29.44	11.84	5.63	6.5	7.75	2.91	1.55	4.96	-	-
No.15	8.45	20.97	27.44	11.84	5.63	6.5	9.75	2.91	1.55	4.96	-	-

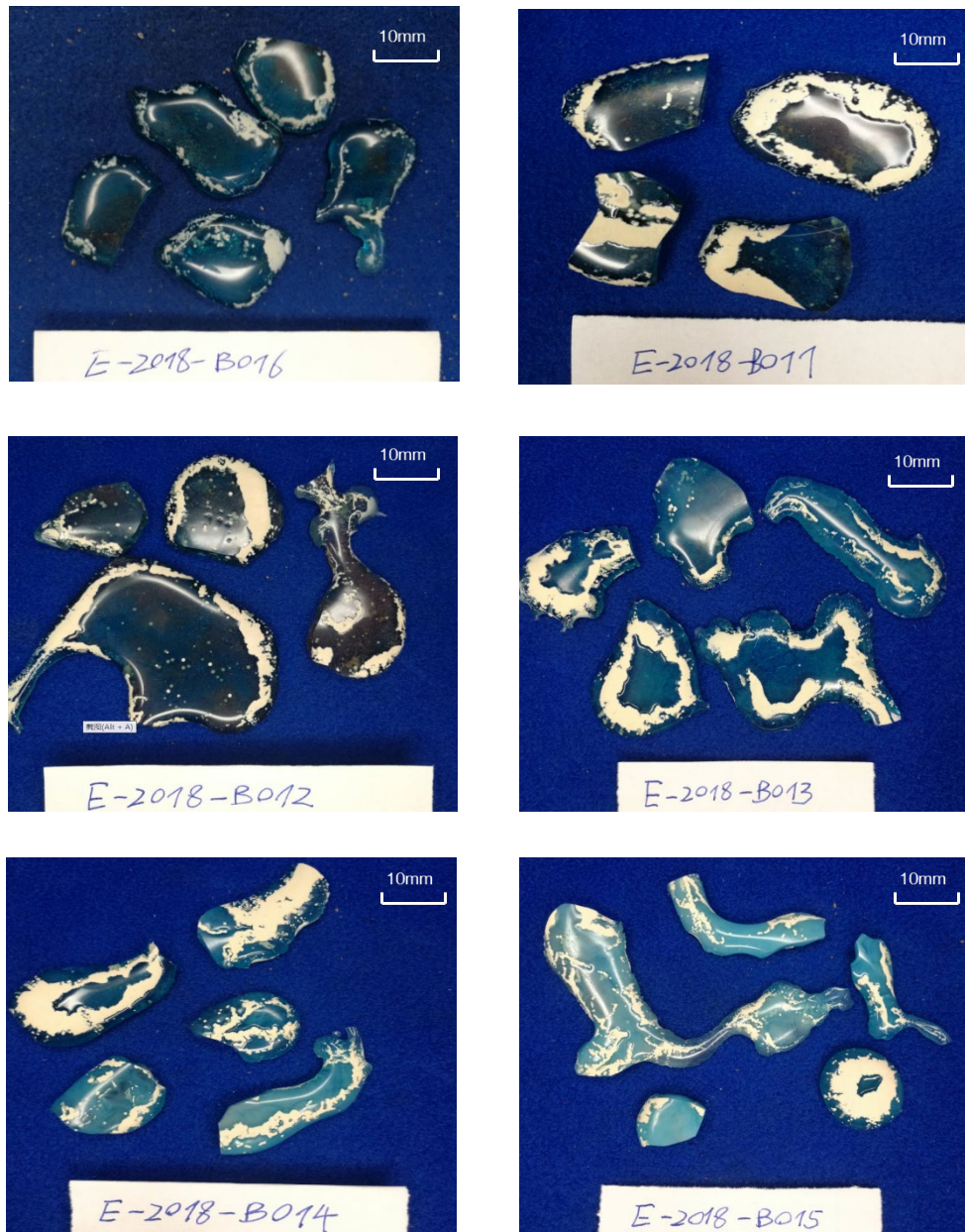


Figure 19: Quenched samples of No.11 to No.16.

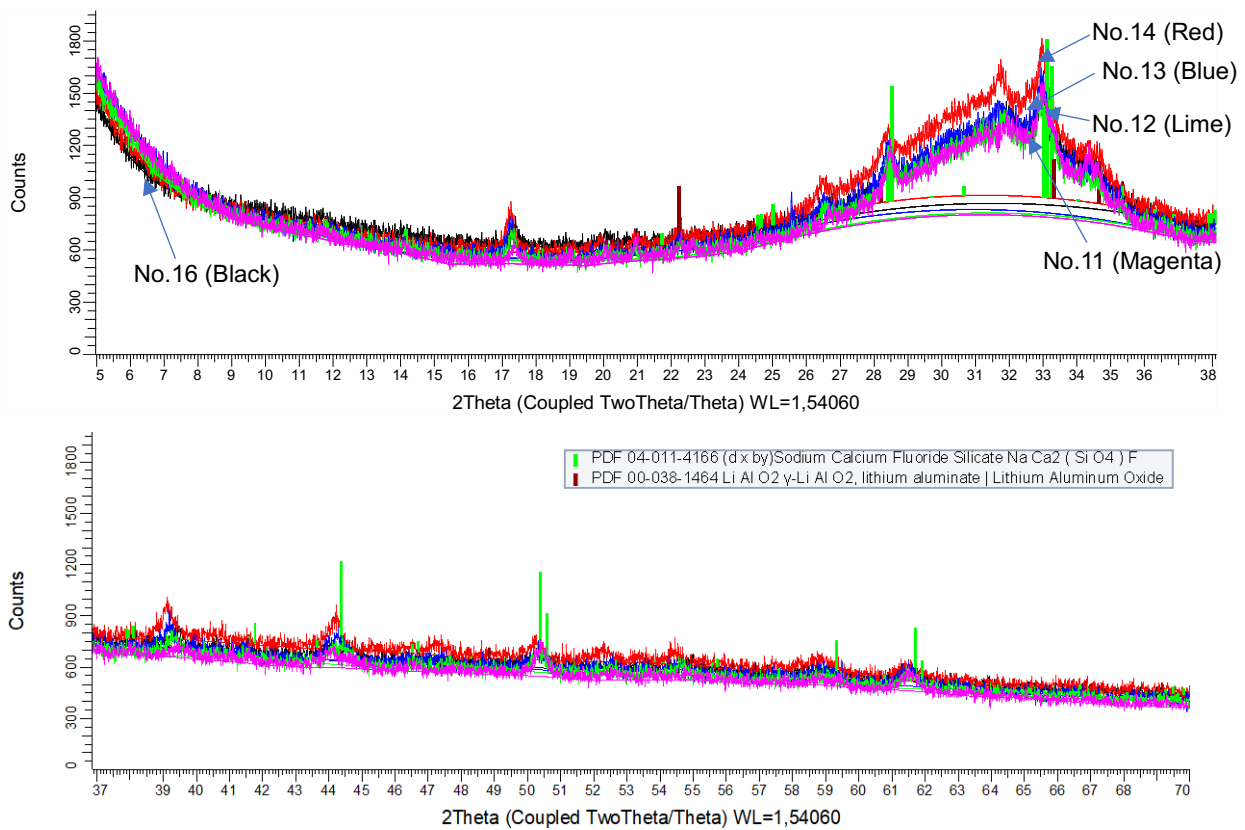


Figure 20: XRD results of quenched samples of No.11, No.12, No.13, No.14 and No.16

4.1.2 Effect on viscosity and break temperature

Sample No.11 to No.16 were measured to analyze the effect of using SrO to substitute CaO on the viscosity of the mould slag. Sample No.12 was tested as well, but the result cannot be used due to serious overflow caused by its relatively high SrO content.

To protect the equipment, only the sample with 1.75 mol% SrO was tested. The results are shown in Figure 21, where the viscosity increases steadily with decreasing temperature until a certain temperature was reached, at which point the viscosity rapidly increases. This particular temperature is defined as the break temperature (T_{br}). The rise in viscosity is due to the crystal formation starting at this temperature during cooling. The replacement of CaO by SrO increases the viscosity from 0.353 Pa·s (No.16) to 0.411 Pa·s (No.11) and slightly decreases the break temperature from 1251 °C (No.16) to 1248 °C (No.11). The measured viscosity at 1300 °C of 0.353 Pa·s is much higher than the calculated of 0.206 Pa·s by FactSage. There were no FactSage results of samples No.11 to No.14 because SrO is not included in the viscosity calculator of FactSage.

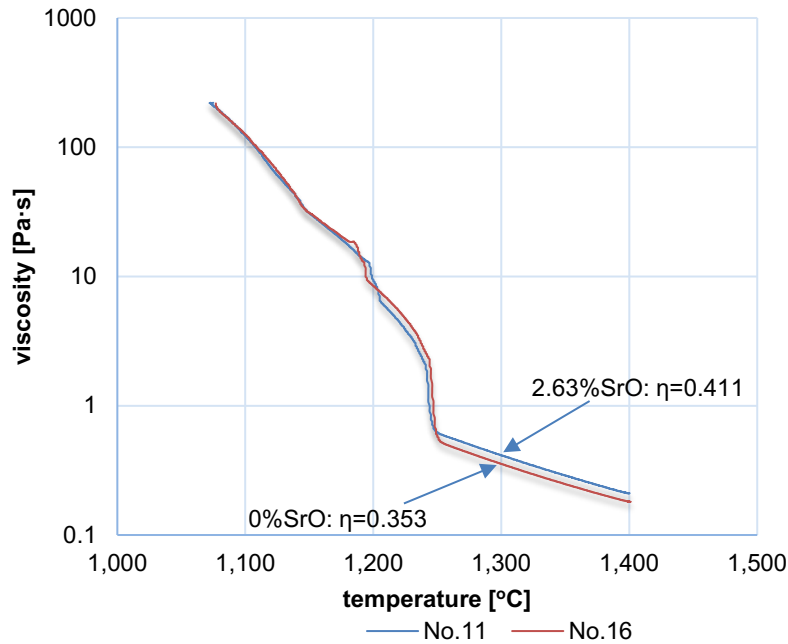


Figure 21: Viscosity of the mould slag

4.1.3 Effect on liquidus temperature, onset of crystallization temperature and mass loss

As shown in Figure 22, there is a sharp exothermal peak at 630.4 °C due to devitrification followed by an endothermal peak at 1004.1 °C. There are 4 more endotherms until the estimated liquidus temperature 1278.9 °C. Furthermore, the mass reduction of mould slag can be found on TG curve, which starts at around 400 °C and sharply increases while the temperature exceeds 1200 °C, ending with a 2.5% mass loss at 1450 °C, which may put the DTA result above 1200 °C in some doubt.

The results of DTA are depicted in Figure 23, 24 and Table 4. Estimated liquidus temperature slightly increases while the SrO content increases. The impact of SrO is rather small since the Sr^{2+} ions can replace Ca^{2+} ions in crystal structures. Due to the evaporation during heating, no liquidus temperature can be given. In this thesis the estimated liquidus temperature was the temperature of the last maximum peak, where the sample is assumed to be liquidus and it is much lower than that calculated by FactSage. Moreover, the minimum crystal form temperature is observed at 1.75 mol% SrO. For mass loss, the exchange of CaO to SrO has little effect on it. FactSage calculated that the first crystalline phase during cooling should be $\text{Na}_2\text{CaAl}_4\text{O}_8$.

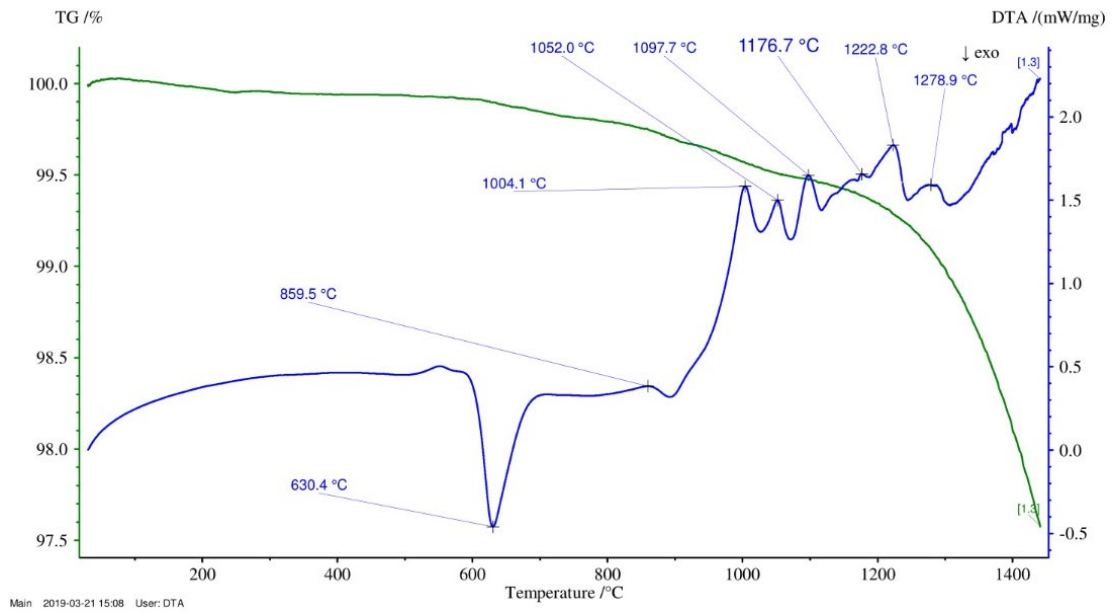


Figure 22: DTA results of sample No.16 during heating

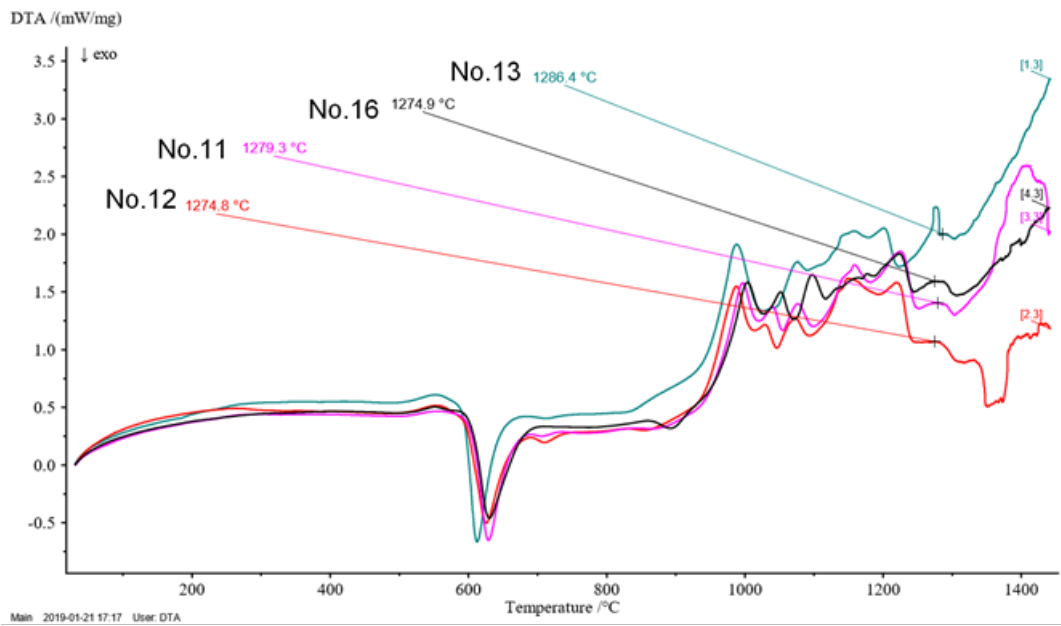


Figure 23: DTA results of sample No.11, No.12, No.13 and No.16 during heating

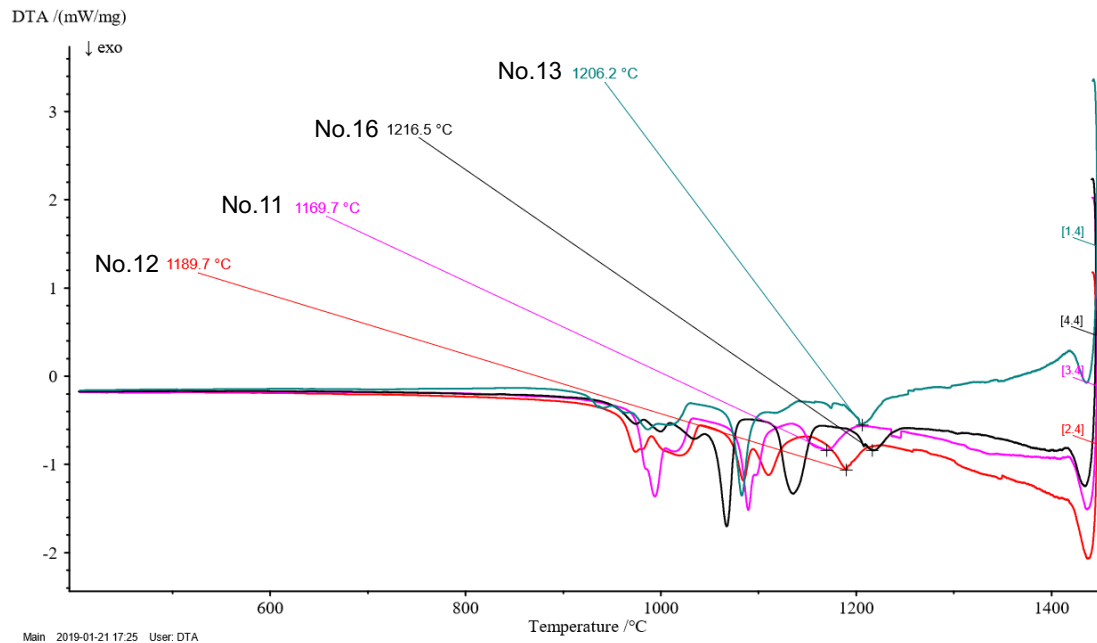


Figure 24: DTA results of sample No.11, No.12, No.13 and No.16 during cooling

Table 4: The results of DTA with varied CaO and SrO content [mole%]

Samples	CaO[mol]	SrO[mol]	Other components	Mass loss [%]	Crystal form temperature[°C]	Estimated liquidus temperature[°C]
No.16	37.15	0	62.85	4.7	1216	1274
No.11	35.44	1.75	62.85	4.5	1169	1279
No.12	33.44	3.75	62.85	5.1	1189	1281
No.13	31.44	5.75	62.85	4.5	1206	1286

4.2 Effect of substituting CaO with MgO

4.2.1 Glass formation of mould slag during quenching

Table 5 shows the chemical composition of sample No.16 and No.20, where sample No.20 used 5 mol% MgO to substitute 5 mol% CaO. After quenching, it can be clearly observed in Figure 25 that the glass formation is favored in No. 16, which means that CaO is better than MgO for glass formation. The XRD results of the quenched samples No.16 and No.20 are shown in Figure 26, which shows more crystal fraction for sample No.20. There are three phases formed during quenching, which are lithium aluminate (Li_5AlO_4), potassium calcium fluoride silicate [$\text{KCa}_7(\text{SiO}_4)_3\text{F}_3$] and calcium fluoride silicate ($\text{Ca}_2\text{SiO}_2\text{F}_2$).

Table 5: Chemical composition of samples No.16 and No.20 [mole%]

Samples	SiO ₂	Al ₂ O ₃	CaO	Na ₂ O	Li ₂ O	CaF ₂	MgO	K ₂ O	TiO ₂	FactSage viscosity [Pa·s]	FactSage liquidus T [°C]
No.16	8.45	20.97	37.15	11.84	5.63	6.5	2.91	1.55	5	0.206	1443
No.20	8.45	20.97	32.15	11.84	5.63	6.5	7.91	1.55	5	0.206	1454

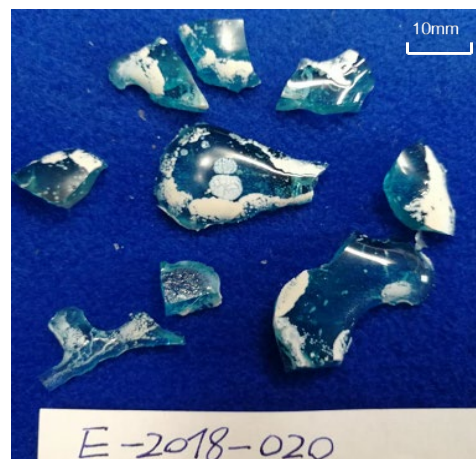
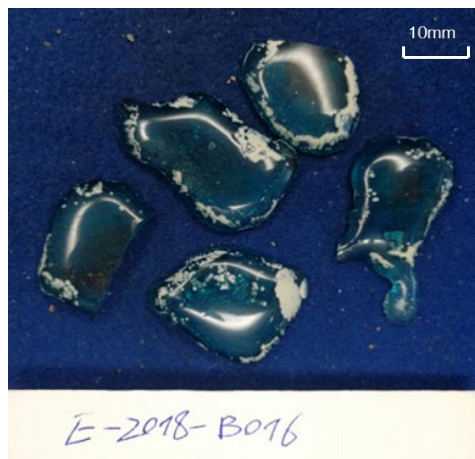


Figure 25: Quenched samples of No.16 and No.20

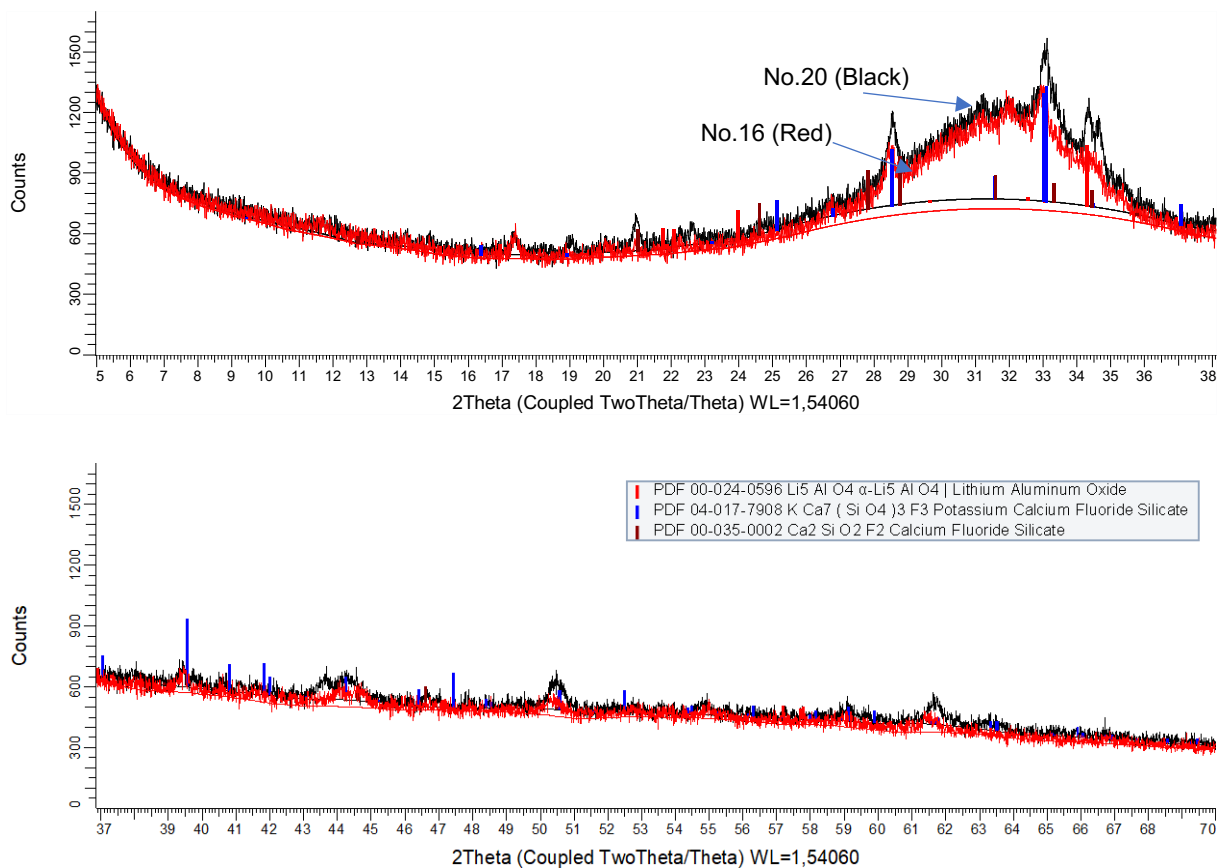


Figure 26: XRD results of quenched sample No.16 and No.20

4.2.2 Effect on liquidus temperature

As shown in Figure 27, compared with sample 16, there is an additional phase formed during heating in sample No.20, which has a higher estimated liquidus temperature (1326 °C). This new phase might be MgO. Therefore, using MgO to substitute CaO may increase the liquidus temperature. As the estimated liquidus temperature exceeds 1300°C, no viscosity measurement was done for the substitution by MgO. In addition, the last peak maximum during melting was much lower than the calculated liquidus temperature by FactSage.

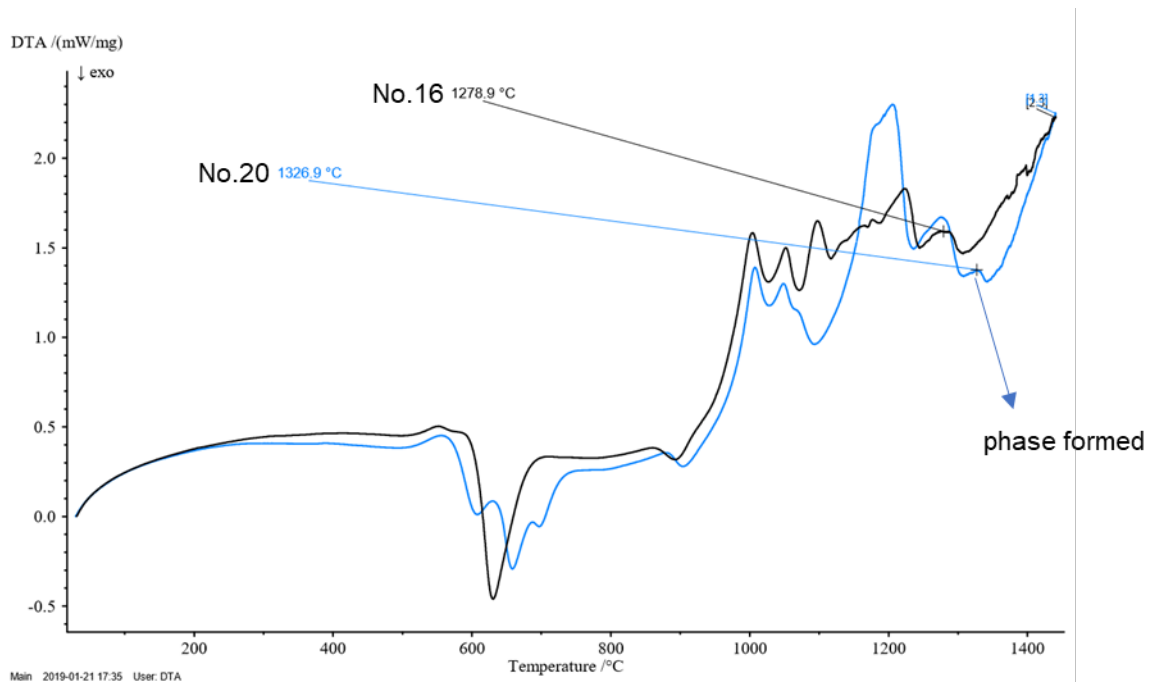


Figure 27: DTA result of sample No.16 and No.20

4.3 Effect of CaF_2

4.3.1 Glass formation of mould slag during quenching

The effect of CaF_2 content on glassy phase formation during quenching can be observed in Figure 28. Sample No.16 containing 6.5 mol% CaF_2 and sample No.21 containing 10.95 mol% have almost the same fraction of crystals, which means that when the CaF_2 content is located between 6.5 mol% to 10.95 mol%, it has little influence on glassy phase formation. However, when the amount of CaF_2 exceeds 10.95 mol%, the crystal fraction increases sharply. XRD results of the quenched samples are shown in Figure 29, it shows that the glass fraction decreases while its content exceeds 10.95 mol%. At the same time, there are some phases formed during quenching, which are potassium calcium fluoride silicate [$\text{KCa}_7(\text{SiO}_4)_3\text{F}_3$], calcium fluoride silicate ($\text{Ca}_2\text{SiO}_2\text{F}_2$), calcium aluminate [$\text{Ca}_3(\text{AlO}_3)_2$], potassium aluminum silicate ($\text{K}_{0.96}\text{AlSiO}_4$) and fluormayenite ($\text{Ca}_6\text{Al}_7\text{O}_{16}\text{F}$).

Table 6: Chemical composition of sample No.16, No.21, No.22, No.23 [mole%]

Samples	SiO ₂	Al ₂ O ₃	CaO	Na ₂ O	Li ₂ O	CaF ₂	MgO	K ₂ O	TiO ₂	FactSage viscosity [Pa·s]	FactSage liquidus T [°C]
No.16	8.45	20.97	37.15	11.84	5.63	6.5	2.91	1.55	5	0.206	1443
No.21	8.05	19.97	35.38	11.28	5.36	10.95	2.77	1.48	4.76	0.148	1429
No.22	7.68	19.06	33.77	10.76	5.12	15	2.65	1.41	4.55	0.115	1415
No.23	7.23	17.94	31.79	10.13	4.82	20	2.49	1.33	4.28	0.092	1398

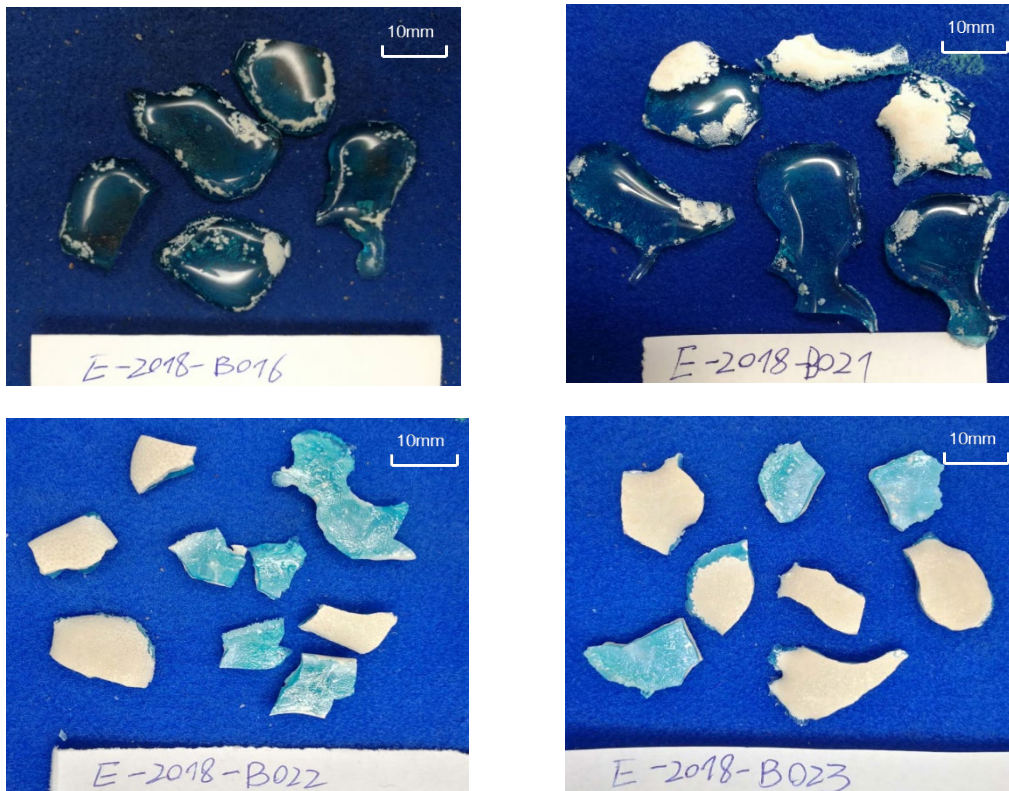


Figure 28: Quenched samples of No.16, No.21, No.22 and No.23

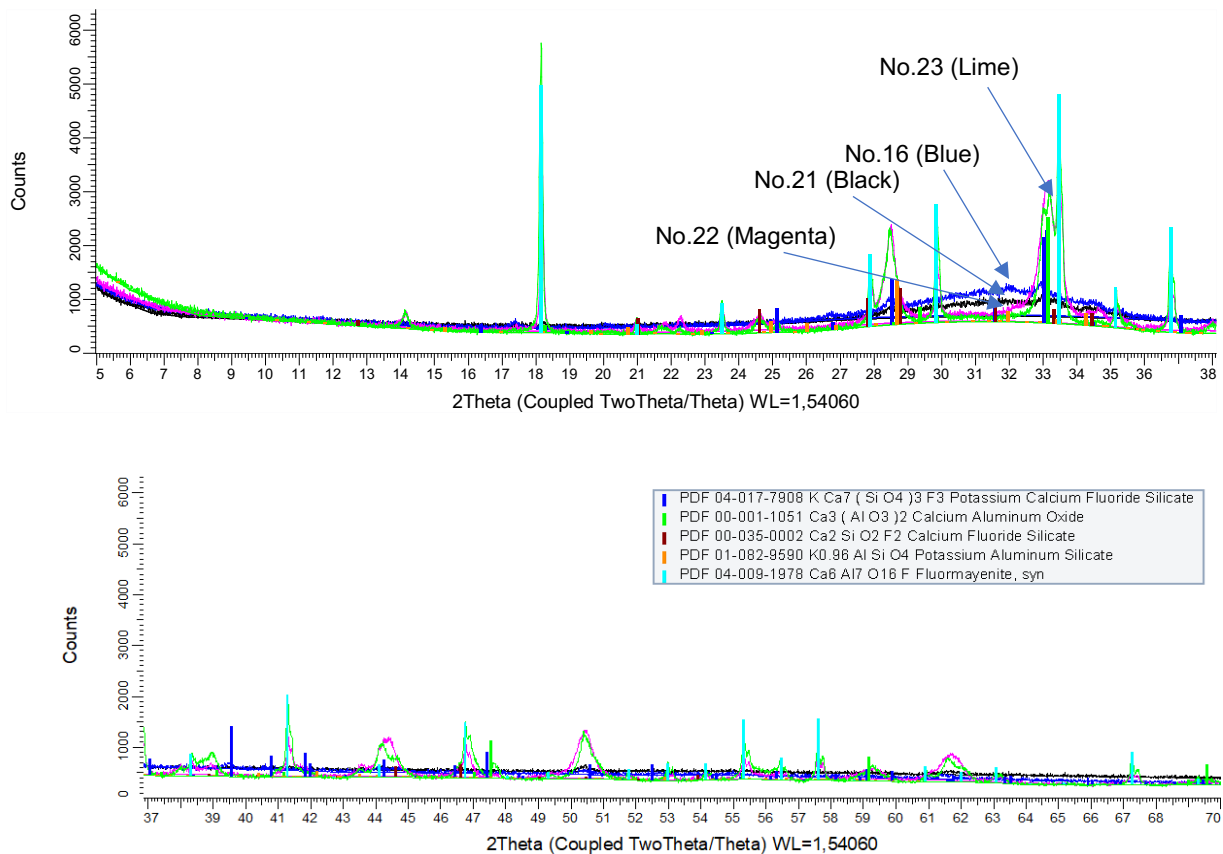


Figure 29: XRD results of quenched sample No.16, No.21, No.22 and No.23

4.3.2 Effect on mass loss

As shown in Figure 30 and Table 7, during heating the mass loss curve starts out stable until the temperature reaches 800 °C, at 1200 °C it drops sharply. This means that the chemical composition is always altered before the sample are totally liquefied around 1275 °C. After the temperature is below 1275 °C during cooling, the mass loss stays stable again. The mass loss of sample increases from 4.7% to 9.6% when the CaF₂ content increases from 6.5% to 20%, which means fluorine could be evaporated. The addition of CaF₂ exceeding 10.95 mol% influences the wetting behavior, because the overflow happened with CaF₂ content above 10.95 mol% as shown in Figure 31. Therefore, crystallization temperature derived by DTA is of doubt.

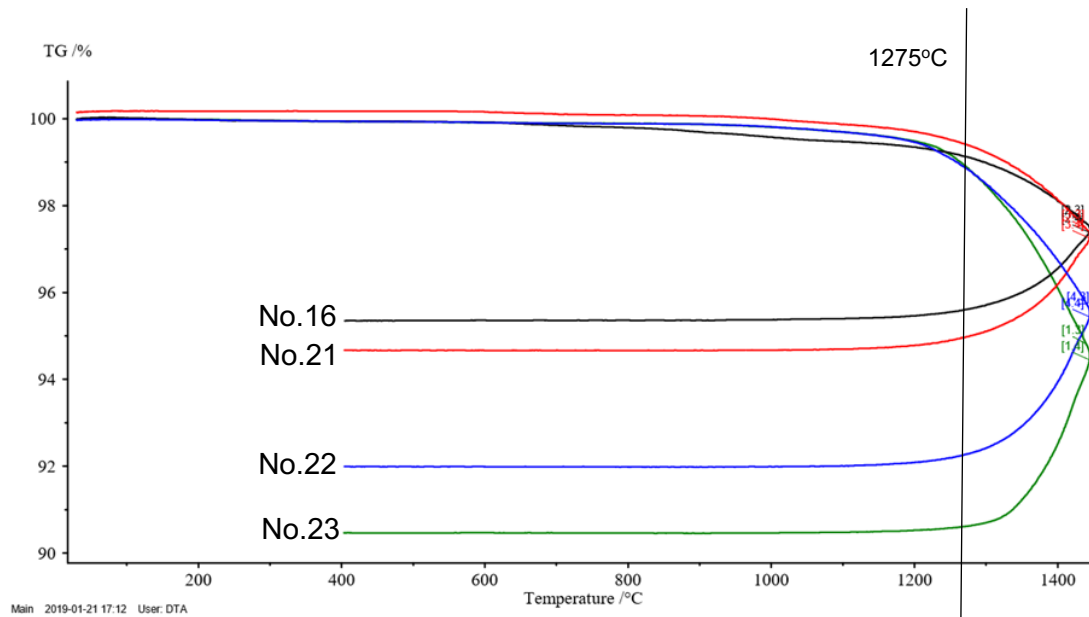


Figure 30: Mass loss of sample No.16, No.21, No.22 and No.23

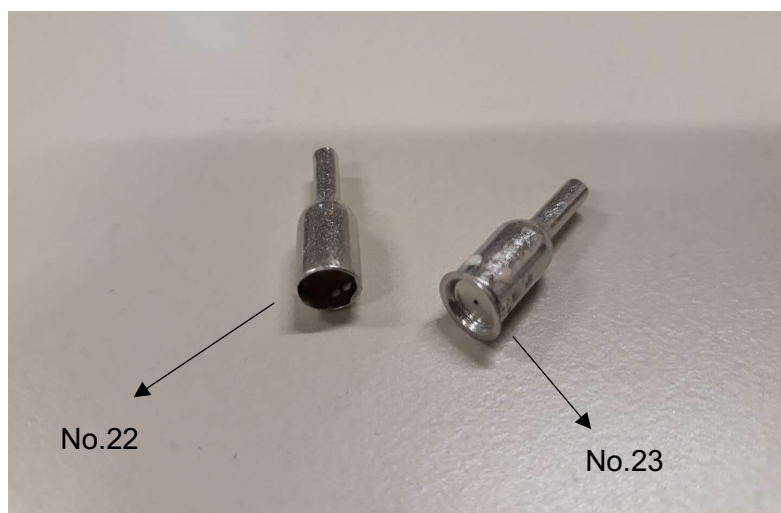


Figure 31: Sample overflow during DTA measurement

4.3.3 Effect on liquidus temperature and onset of crystallization temperature

The samples with different CaF_2 content were tested by DTA, the results are shown in Figure 32 and Table 7, where it can be clearly observed that the peak temperature of the last endothermic peak during heating of the mould slag decreases first and then increases with increasing CaF_2 content. Sample No.21 containing 10.95 mol% CaF_2 has the lowest estimated liquidus temperature. When the CaF_2 content exceeds 15 mol%, it has little effect on the liquidus temperature. In FactSage, with the addition of CaF_2 content, it shows a continuous decrease of the liquidus temperature. This is not apparent in the DTA curves. The calculated first phase to crystallize during cooling

is $\text{Na}_2\text{CaAl}_4\text{O}_8$.

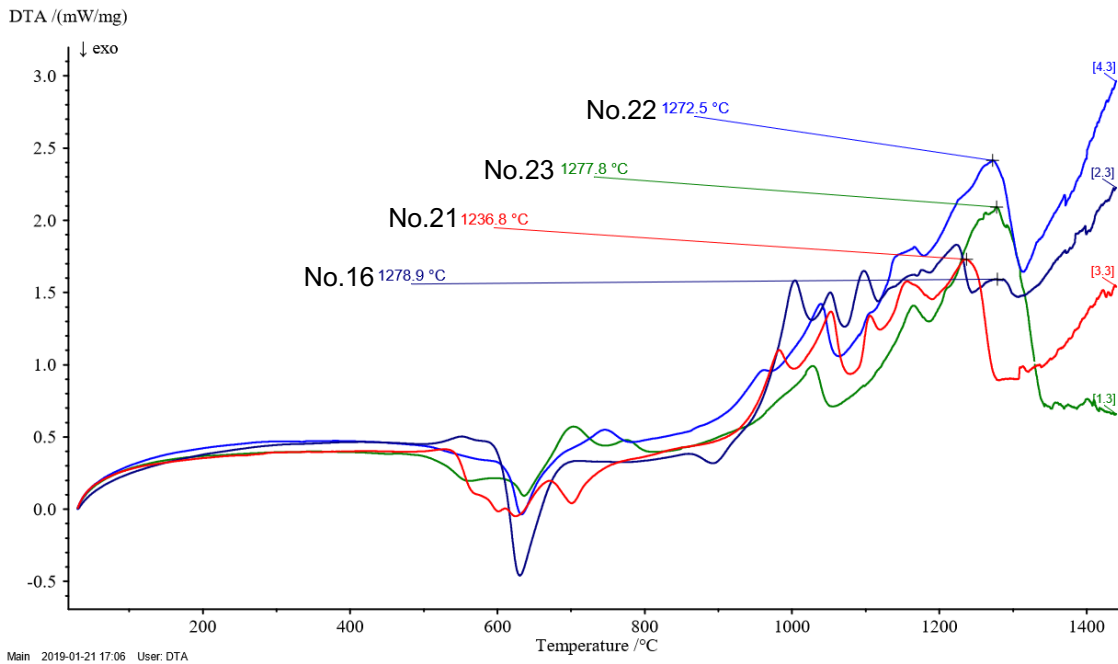


Figure 32: DTA results of sample No.16, No.21, No.22 and No.23 during heating

As shown in Figure 33 and Table 7, with the CaF_2 content increases, the first crystallization temperature decreases first and then increases during cooling. Compared with sample No.16, sample No.21 lost one phase which corresponds to the first exothermic peak at 1216 °C. However, due to the evaporation behavior during DTA, these results are of doubt.

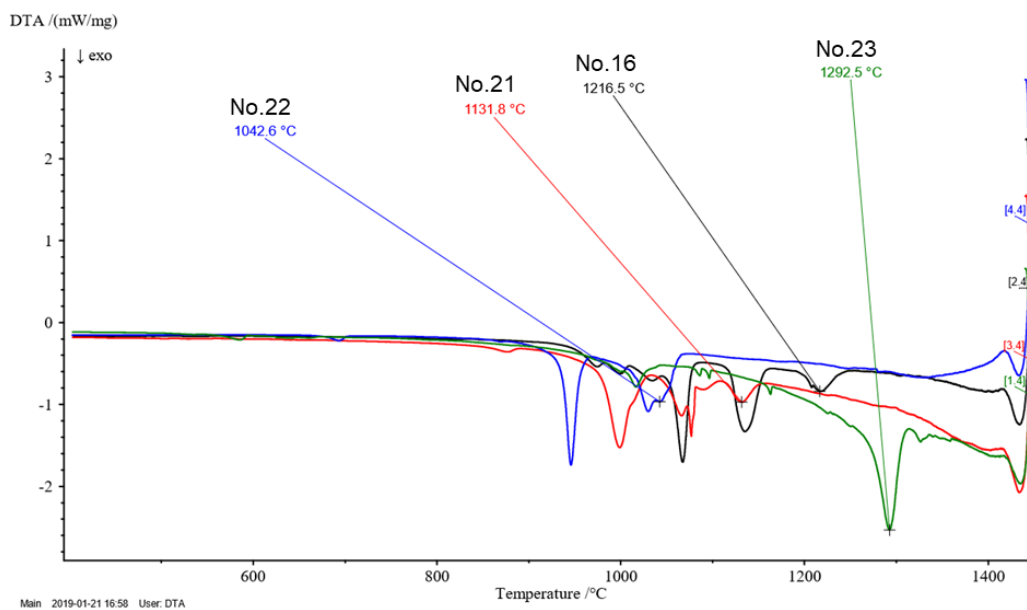


Figure 33: DTA results of sample No.16, No.21, No.22 and No.23 during cooling

Table 7: The results of DTA with varied CaF₂ content

Samples	CaF ₂ [mol]	Other fluxes	Mass loss [%]	Estimated liquidus temperature[°C]	Crystal form temperature[°C]
No.16	6.50	93.50	4.7	1274	1216
No.21	10.95	89.05	5.3	1236	1131
No.22	15	85	8.0	1272	1042
No.23	20	80	9.6	1277	1292

4.3.4 Effect on the viscosity

As aforementioned, the sample could overflow in the crucible during heating. Therefore, only for samples No.16 and No.21 the viscosity was tested as shown in Figure 34 and Table 8. With the CaF₂ content increasing from 6.50 mol% to 10.95 mol%, the viscosity at 1300 °C decreases from 0.353 Pa·s to 0.283 Pa·s, and the T_{br} decreases from 1251 °C to 1213 °C. CaF₂ has a desirable effect on the decrease of viscosity and break temperature of the slag. Unfortunately, due to the overflow, the impact of high CaF₂ content could not be worked out.

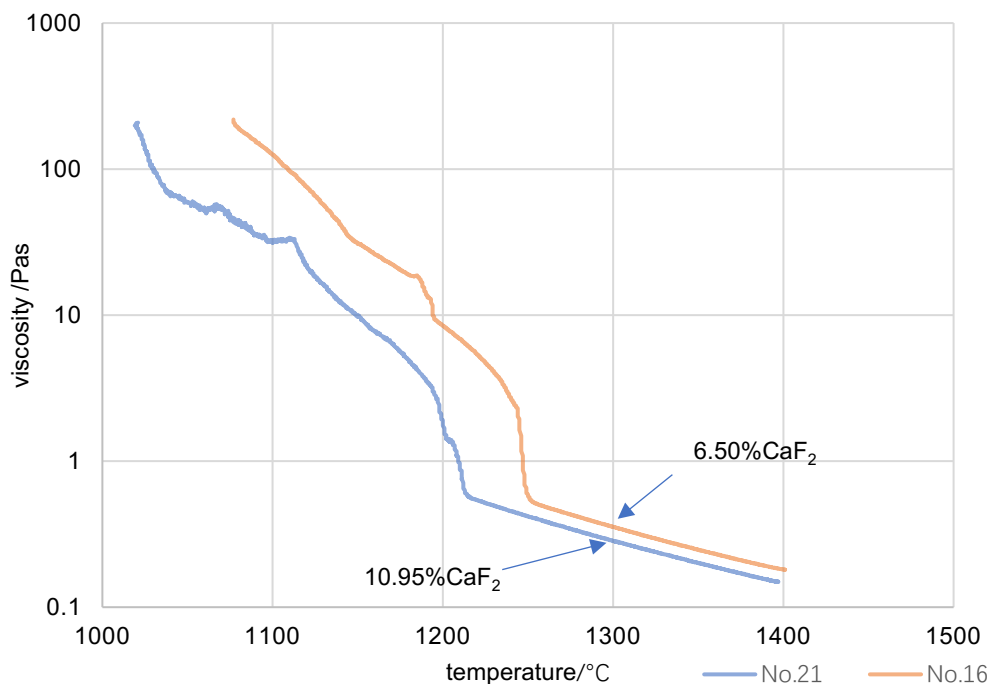


Figure 34: Temperature-viscosity curve of sample No.16 and No.21

Table 8: The results of viscosity at 1300 °C and T_{br} of sample No.16 and No.21

Samples	CaF ₂ [mol]	Other fluxes[mol]	viscosity at 1300°C [Pa·s]	Break temperature [°C]
No.16	6.5	93.5	0.353	1251
No.21	10.95	89.05	0.283	1213

4.3.5 Phase formation

The sample No.21 was analyzed by furnace crystallization test. After the slow cooling, XRD and SEM test are applied to identify the phase formation as shown in Figure 35 and 36. It is a complex crystalline microstructure and without any glassy phase. According to FactSage, Na₂CaAl₄O₈ is the first precipitating phase out of the melt. This phase cannot be verified by SEM and XRD.

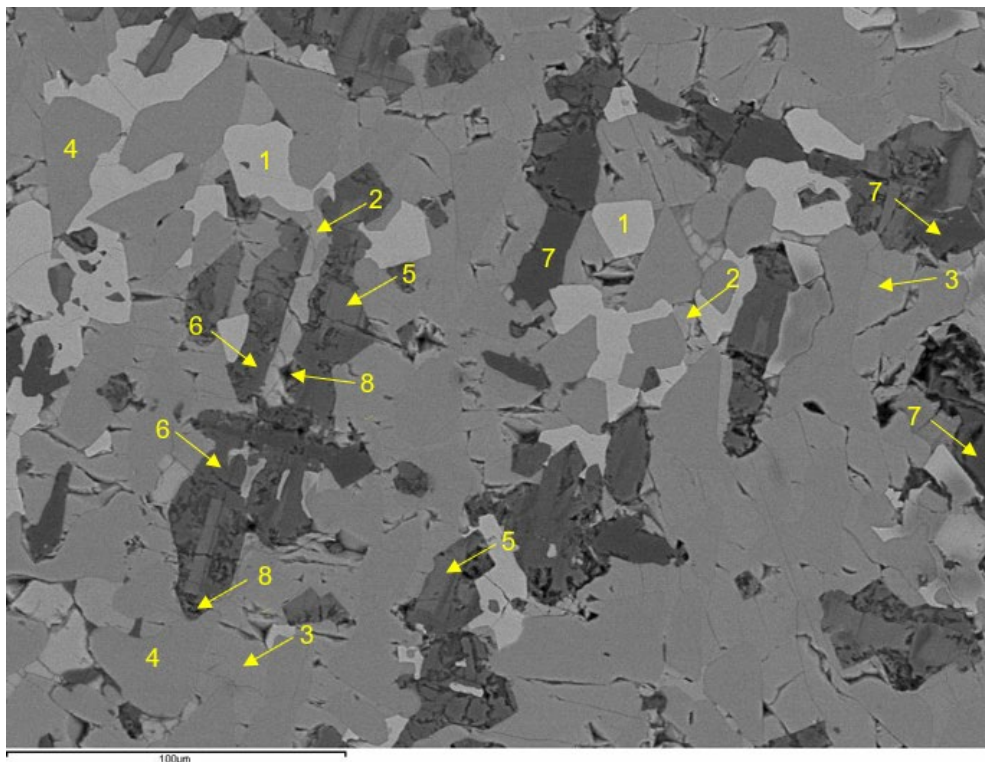


Figure 35: Backscattered electron image of sample No.21 after furnace crystallization test

- 1...Perovskite ($\text{Ca}(\text{Ti,Fe,Al,Si})\text{O}_3$)
- 2...Calcium fluoride (CaF_2)
- 3...Sodium calcium fluoride silicate ($\text{NaCa}_2\text{SiO}_4\text{F}$)
- 4...Calcium aluminum silicate ($\text{Ca}_6\text{Al}_5\text{Si}_2\text{O}_{17.5}$)
- 5...Sodium calcium aluminate ($\text{Ca}_3\text{Na}_4\text{Al}_{10}\text{O}_{20}$)

- 6...Sodium aluminate (NaAlO_2)
- 7...Lithium aluminate (LiAlO_2)
- 8...Potassium containing phase

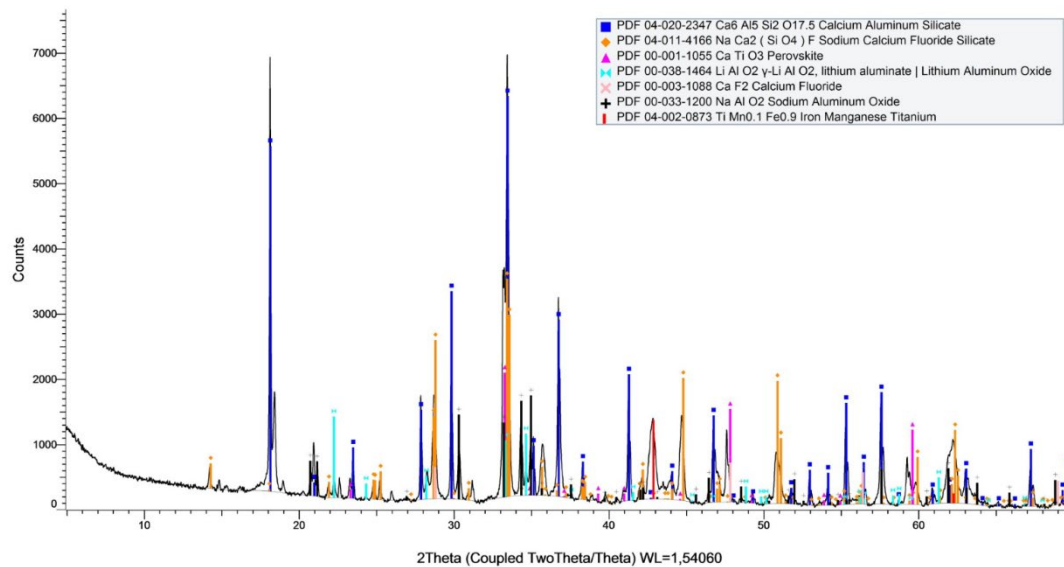


Figure 36: XRD result of FCT sample No.21

4.4 Effect of Li_2O

4.4.1 Glass formation of mould slag during quenching

Figure 37 shows the compositions of quenched mould slag samples that have varied Li_2O content. It can be clearly observed that the Li_2O content seriously affects the glassy phase formation. With the decrease of Li_2O content from 5.36 mol% to 0.86 mol%, the glassy phase fraction decreases. There is a sharp glassy phase fraction reduction from sample No.21 to No.24, which means that the Li_2O content between 5.36 mol% and 3.86 mol% strongly affects the glassy phase formation. Continued decrease of the Li_2O content slightly reduces the glassy phase formation. The XRD results of the quenched samples are shown in Figure 38, it showed that the glass fraction decreases with the decrement of Li_2O content. Fluormayenite ($\text{Ca}_6\text{Al}_7\text{O}_{16}\text{F}$), calcium fluoride silicate ($\text{Ca}_2\text{SiO}_2\text{F}_2$) and calcium aluminate ($\text{Ca}_3\text{Al}_2\text{O}_6$) are formed during quenching.

Table 9: Chemical composition of samples [mole%]

Samples	SiO ₂	Al ₂ O ₃	CaO	Na ₂ O	Li ₂ O	CaF ₂	MgO	K ₂ O	TiO ₂	FactSage viscosity [Pa·s]	FactSage liquidus T [°C]
No.21	8.05	19.97	35.38	11.28	5.36	10.95	2.77	1.48	4.76	0.148	1443
No.24	8.18	20.29	35.94	11.46	3.86	11.13	2.82	1.50	4.84	0.154	1439
No.25	8.30	20.60	36.50	11.63	2.36	11.30	2.86	1.52	4.91	0.162	1449
No.26	8.43	20.92	37.06	11.81	0.86	11.47	2.90	1.55	4.99	0.171	1463

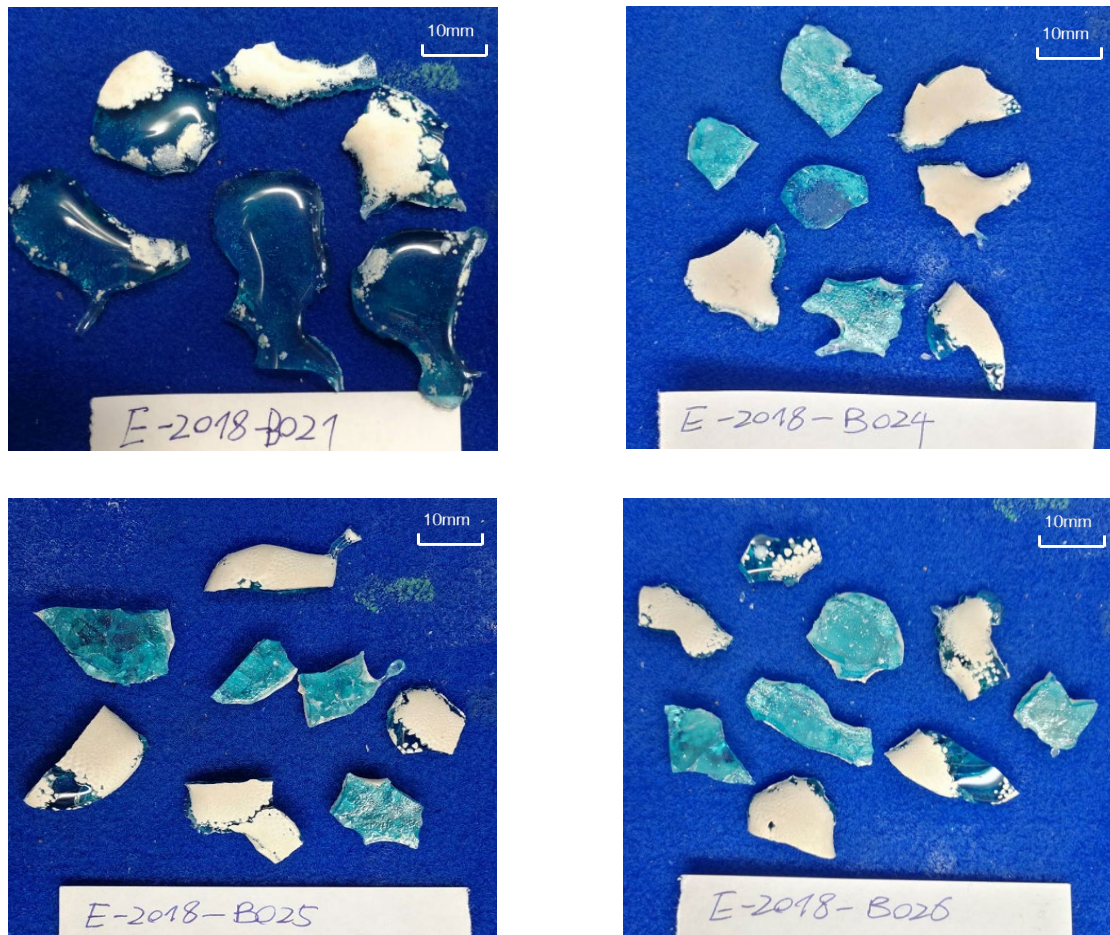


Figure 37: Quenched samples of No.21, No.24, No.22 and No.23

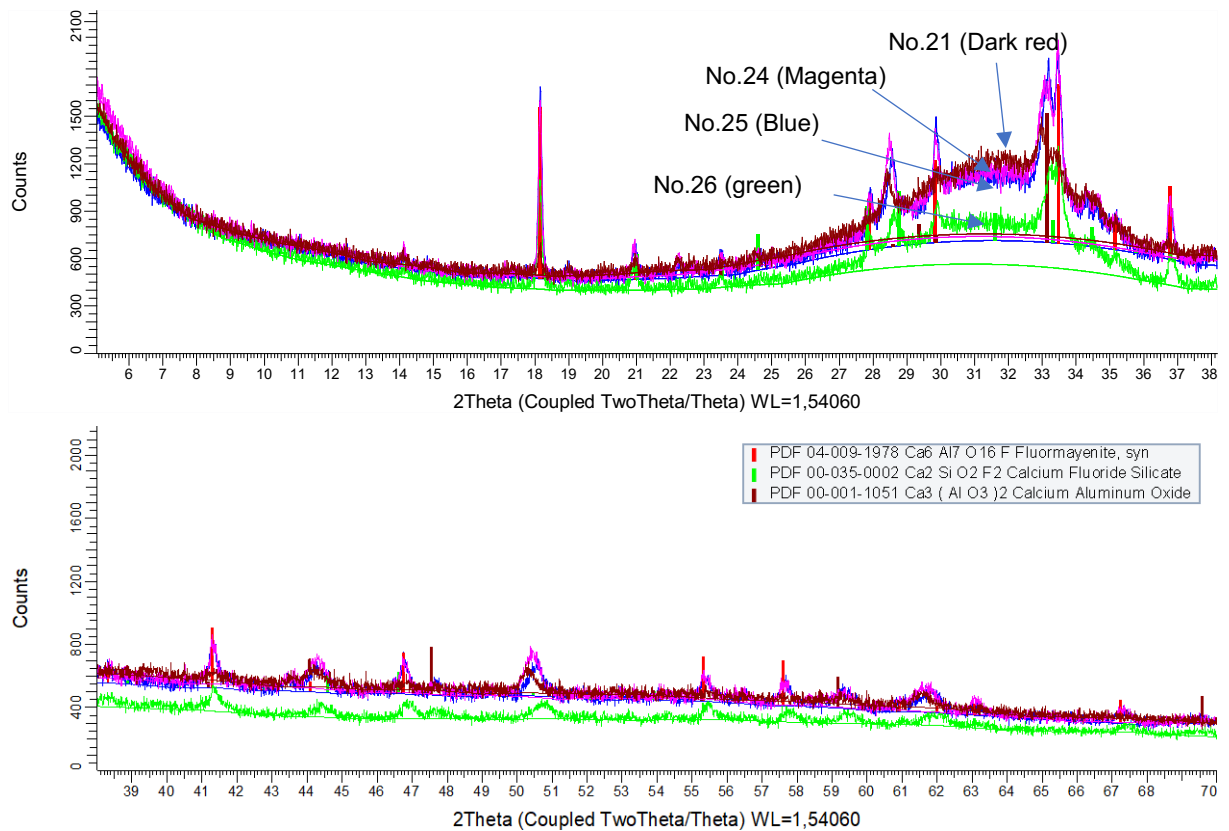


Figure 38: XRD results of quenched sample No.21, No.24, No.25 and No.26

4.4.2 Effect on viscosity and break temperature

The viscosity results are shown in Figure 39 and 40, where it can be clearly observed that with the Li_2O content increasing from 0.86 mol% to 5.36 mol%, the viscosity decreases from 0.428 Pa·s to 0.283 Pa·s, and the break temperature decreases from 1280 °C to 1213 °C. Therefore, addition of Li_2O could decrease the viscosity and break temperature of the slag. Comparing with the FactSage calculated results, the measured viscosities are much higher.

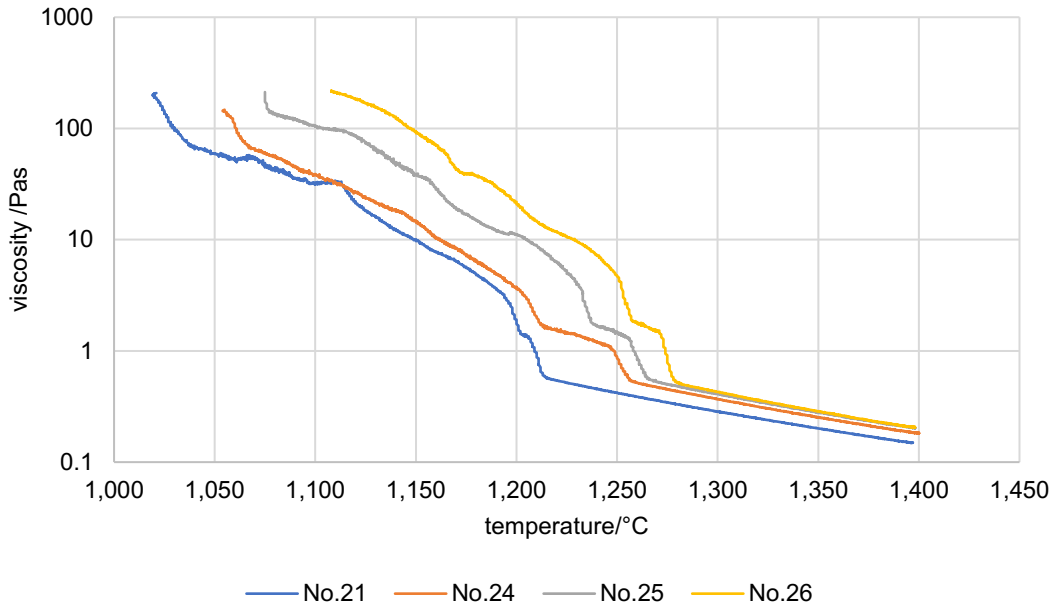


Figure 39: Temperature-viscosity curve of samples

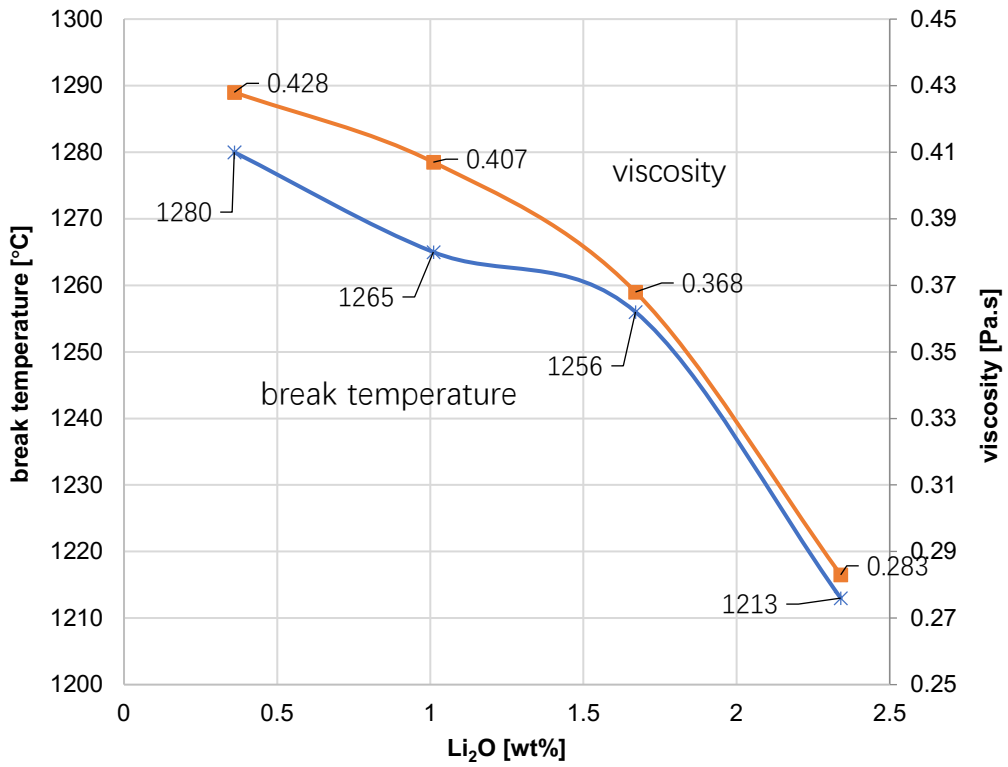


Figure 40: Viscosity (at 1300 °C) - Li₂O content and T_{br} - Li₂O content curve

4.4.3 Inclined plane test to estimate the viscosity

The inclined plane test was conducted to estimate the viscosity of the sample. The results are shown in Table 10. The lengths of slag ribbons are proportional to the measured viscosities of the mould slags except for sample No.24 which may result from test deviation.

Table 10: Inclination plane test result of sample No.21, No.24, No.25, No.26

	Mass [g]	Mean temperature [°C]	Mean length [mm]	Mean residual [g]	Viscosity [Pa·s]
No.21	15	1279	253	2.5	0.283
No.24	15	1265	258	2.5	0.368
No.25	15	1289	237	2.5	0.407
No.26	15	1263	232	2.8	0.428

4.4.4 Effect on liquidus temperature and crystallization temperature

From the DTA results, the estimated liquidus temperatures are shown in Figure 41 and Table 11. With the Li_2O content decreasing from 5.86 mol% to 0.86 mol%, the maximum peak temperature of the last endothermic peak during heating increases from 1236.8 °C to 1298.5 °C, which means that the Li_2O content has a strong effect on the estimated liquidus temperature of the mould slag. Also, the measured liquidus temperature is much lower than the FactSage calculated liquidus temperature. The calculated first crystallized phase during cooling is $\text{Na}_2\text{CaAl}_4\text{O}_8$. For crystal formation temperature and mass loss of the sample, they do not have a linear relationship with the Li_2O content. The minimum crystal formation temperature is observed at 3.86 mol% Li_2O (Figure 42).

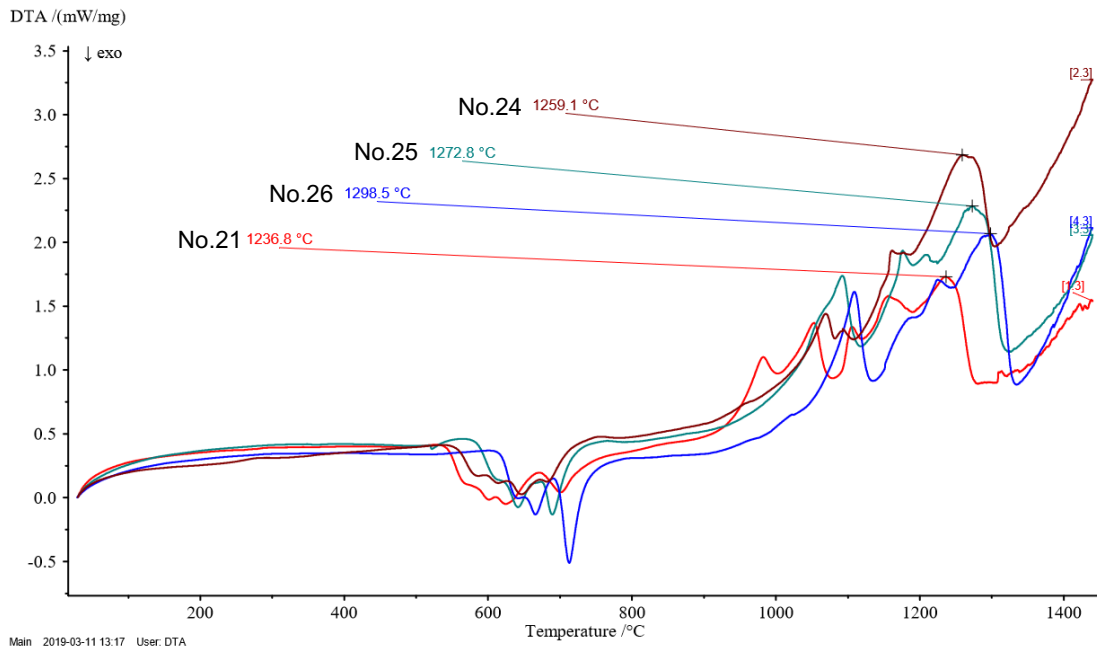


Figure 41: DTA results of sample No.21, No.24, No.25 and No.26 during heating

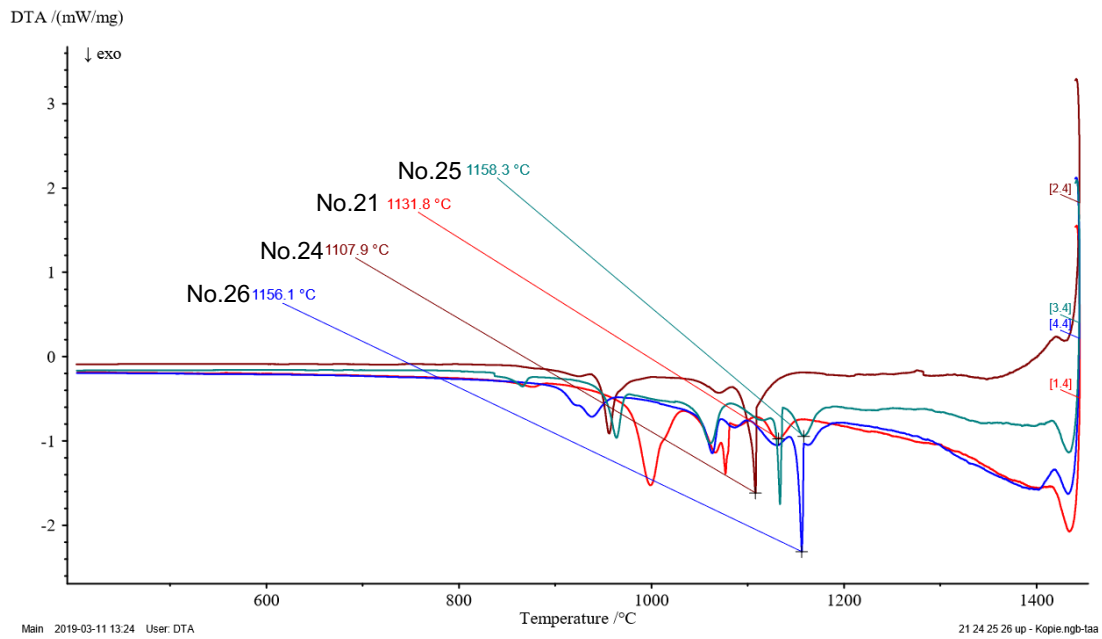


Figure 42: DTA results of sample No.21, No.24, No.25 and No.26 during cooling

Table 11: The results of DTA with varied Li₂O content

Samples	Li ₂ O [mol]	Other fluxes		Estimated liquidus temperature [°C]	Crystal form temperature[°C]
		[mol]	Mass loss [%]		
No.21	5.36	94.64	5.2	1236	1131
No.24	3.86	96.14	8.8	1259	1107
No.25	2.36	97.64	5.9	1272	1158
No.26	0.86	99.14	5.5	1298	1156

4.4.5 Single hot thermocouple technique (SHTT) to analyze the crystallization behavior

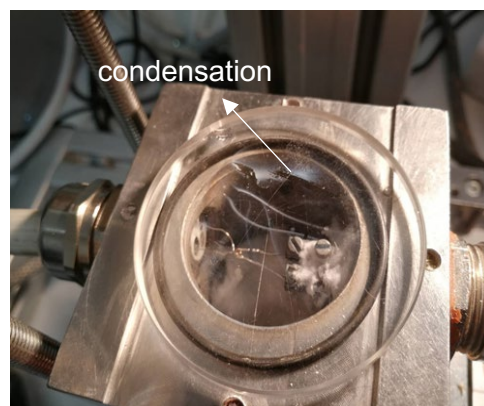
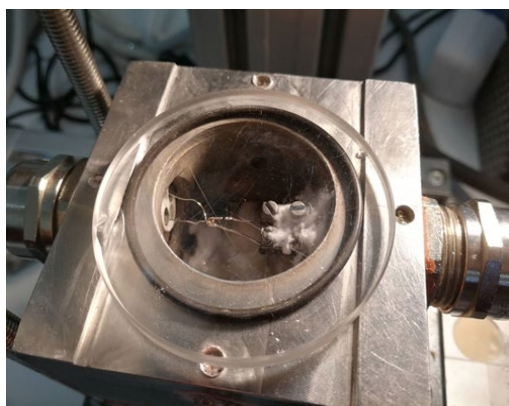


Figure 43: Before feeding the sample (No.21) Figure 44: After feeding the sample (No.21)

SHTT was utilized to analyze the influence of crystallization behavior of sample No.21. Although the estimated liquidus temperature is 1237 °C, the sample was not completely liquidus at a given wire temperature of 1300°C. Therefore, the sample was heated up to 1400 °C. However, a part of the mould powder evaporated rapidly at this temperature on the hot wires due to the high specific surface, which can be seen in Figure 43 and Figure 44. The white solid attached to the glass is composed of evaporated powder. This will most likely be fluorine, Na₂O and Li₂O. Therefore, it is not possible to get a reasonable result. Two trials were performed. One was conducted at a fixed temperature of 1300 °C, the crystallization was visible in a short time. For the other trial the temperature was fixed at 800 °C, with stretching and cooling being performed at the same time. No crystallization could be detected in a short time, which means that the nose of T-T-T curve is at relatively high temperature.

4.4.6 High temperature quenching from 1400 °C to 900 °C

The samples No.21, No.24, No.25 and No.26 were quenched from 1400 °C to 900 °C with different dwell periods as shown in Figure 45. With decreasing Li_2O content, the color of the samples shifts from light blue to sand yellow. For the same composition with different dwell period, there are not much difference in color.

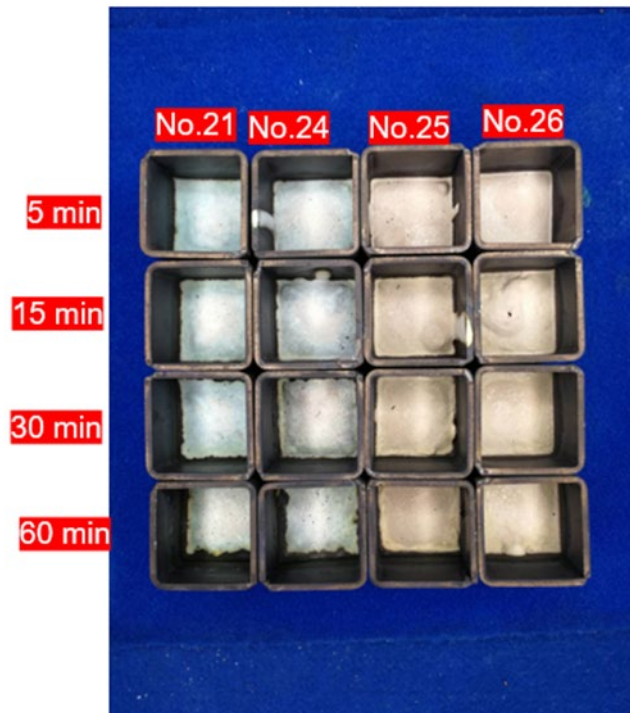


Figure 45: Quenched samples of No.21, No.24, No.25 and No.26 from 1400 °C to 900 °C

Polished sections were prepared from the samples shown above. The optical microscope was used to observe the crystal size. Take sample No.21 for example, the crystal size increases while the dwell period increases which can be seen in Figure 46, which is also observed for samples No.24, No.25, No.26 (Figure A-1, A-2 and A-3). For the constant dwell period 15 min, with decreasing Li_2O content, the crystal size decreases as shown in Figure 47 and 48; the same applies for dwell times of 5 min, 30 min, 60 min (Figure A-4, A-5 and A-6).

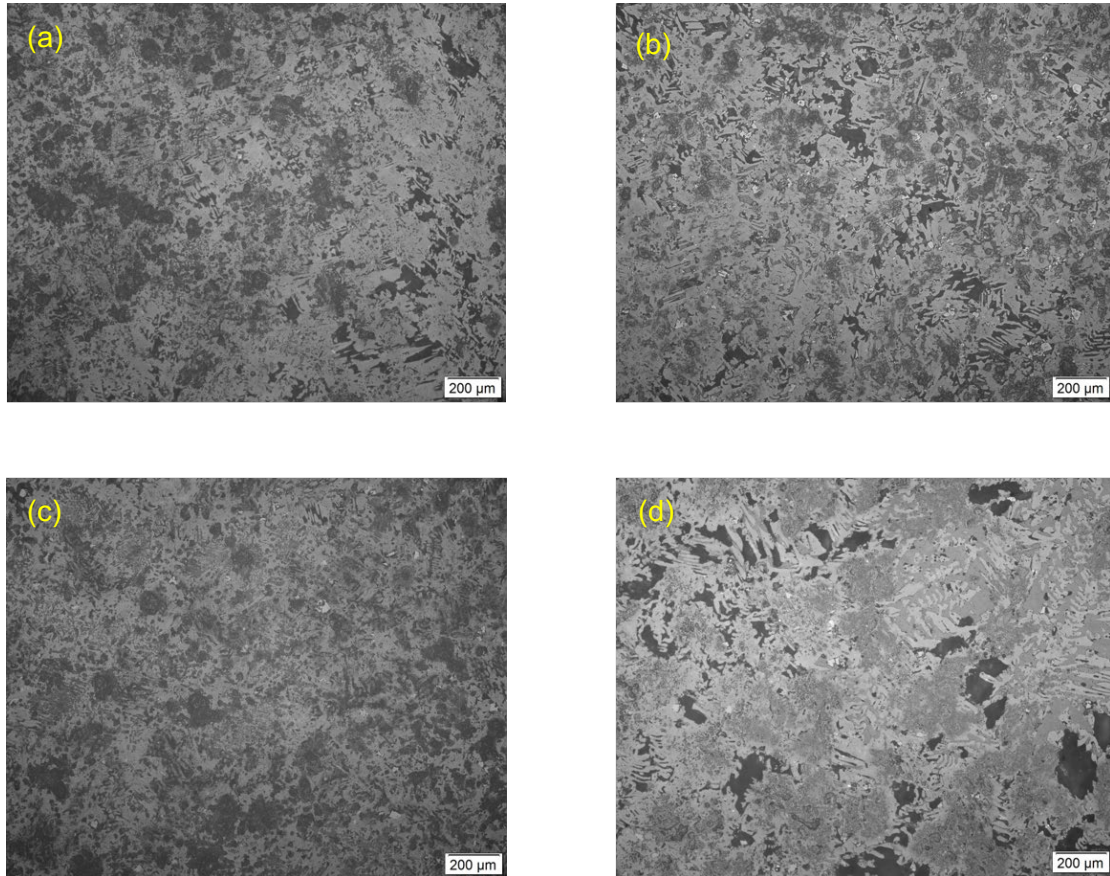


Figure 46: Optical micrographs; a) of sample No.21 dwell 5 min; b) of sample No.21 dwell 15 min; c) of sample No.21 dwell 30 min; d) of sample No.21 dwell 60 min; From (a) to (d) the crystal size increases with increasing dwell period.

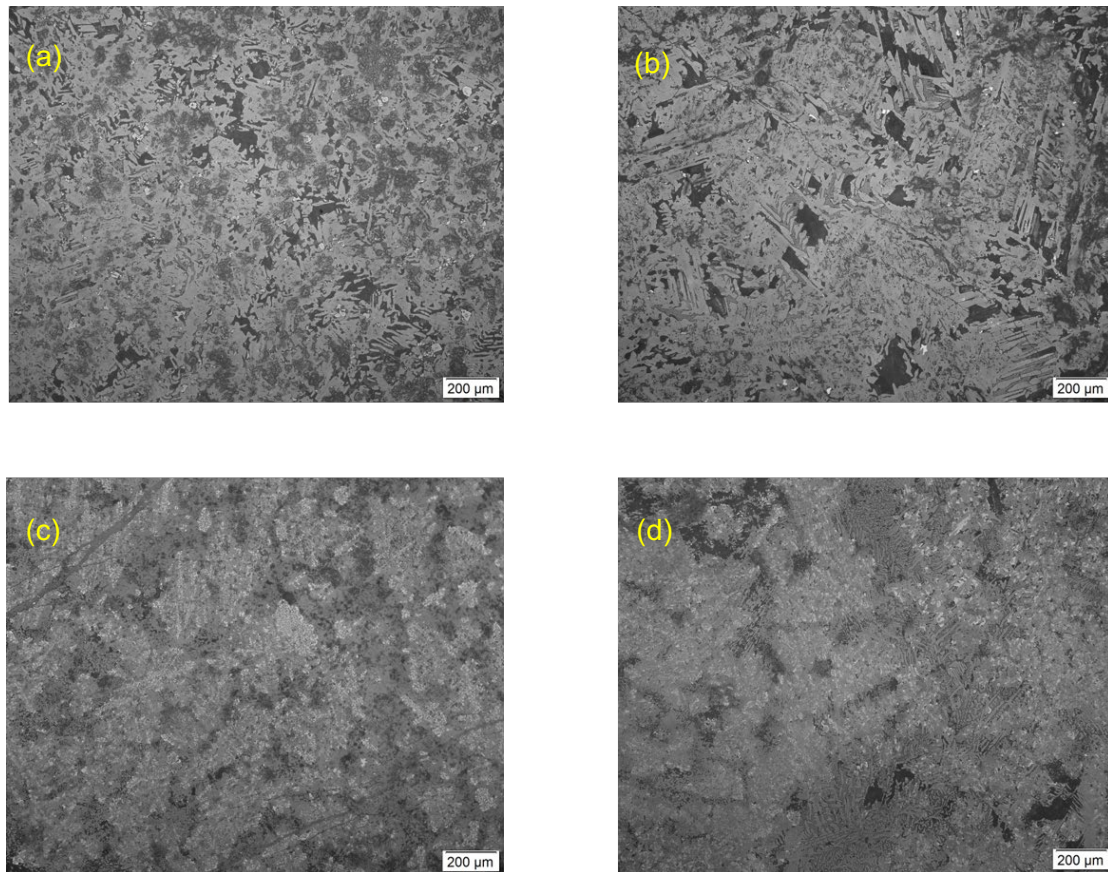


Figure 47: Optical micrographs; a) of sample No.21 dwell 15 min; b) of sample No.24 dwell 15 min; c) of sample No.25 dwell 15 min; d) of sample No.26 dwell 15 min; From (a) to (d) the crystal size decreases with increasing Li_2O content.

For example, in Figure 46 and 49, the results for the quenched sample No.21 with different dwell period are given. It is a complex crystalline microstructure and without any glass phase. For sample No.21 with different dwell period, the XRD curve are almost the same. The small difference is caused by the different contents of LiAlO_2 as shown in Figure 50. The phase content of LiAlO_2 decreases with the increment of the dwell period from 5 min to 60 min. With samples No.24, 25 and 26, similar effects are visible in the XRD curves (Figure A-7, A-8 and A-9).

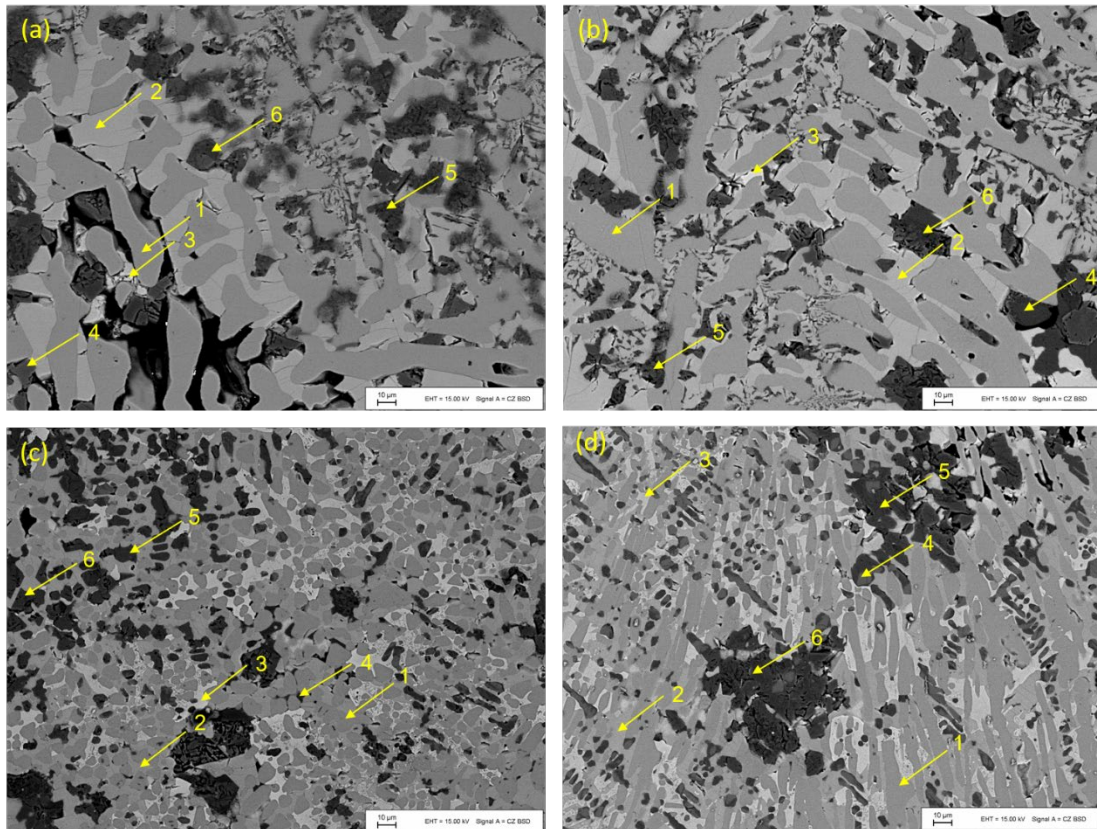


Figure 48: Backscattered electron images of samples; a) of No.21 dwell 15 min; b) of sample No.24 dwell 15 min; c) of sample No.25 dwell 15 min; d) of sample No.26 dwell 15 min;

- 1... Sodium calcium aluminate ($\text{Ca}_3\text{Na}_4\text{Al}_{10}\text{O}_{20}$)
- 2... Sodium calcium fluoride silicate solid solution ($\text{NaCa}_2\text{SiO}_4\text{F}$)
- 3... Calcium aluminum silicate solid solution ($\text{Ca}_6\text{Al}_5\text{Si}_2\text{O}_{17.5}$)
- 4... Villiaumite (NaF)
- 5... Sodium aluminate (NaAlO_2)
- 6... Lithium aluminate (LiAlO_2)

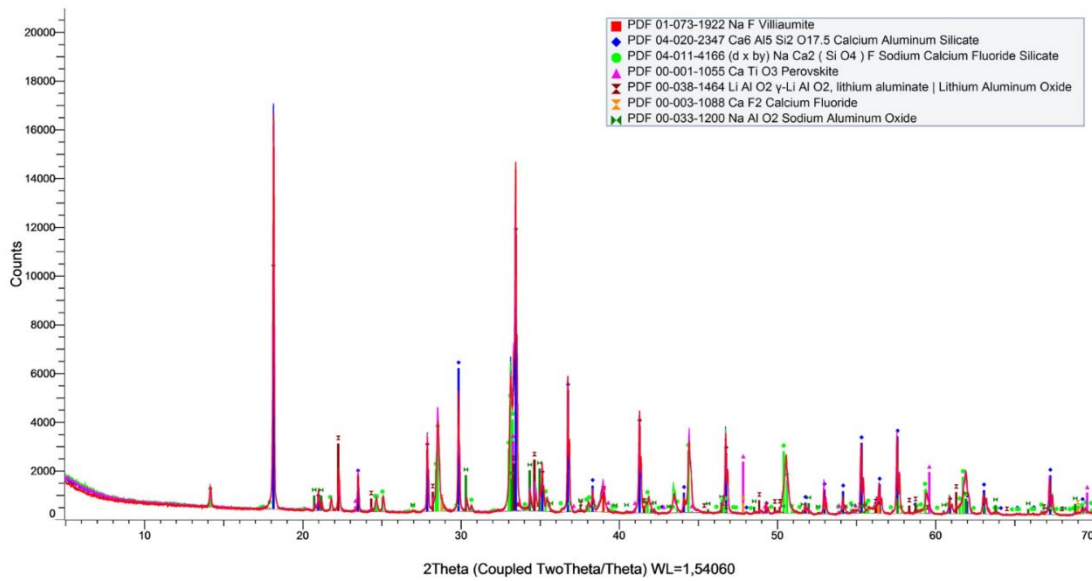


Figure 49: XRD result of sample No.21 with dwell period 5 min, 15 min, 30 min and 60 min

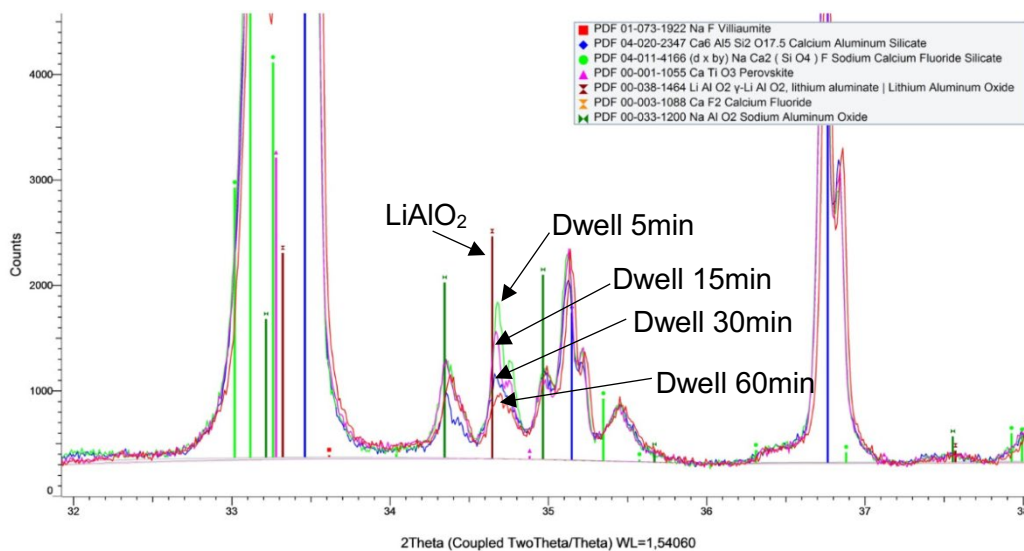


Figure 50: XRD result of LiAlO_2 content change in sample No.21 with dwell period 5 min, 15 min, 30 min and 60 min

The XRD results of samples No.21, No.24, No.25 and No.26, which contain different contents of Li_2O with the same dwell period of 15 min are shown in Figure 51. The XRD curves almost coincide, which means that the samples have the same phases. However, there are some peaks which have different height as shown in Figure 52. This peak response for LiAlO_2 , and the height is related to its content. Therefore, the phase content of LiAlO_2 decreases with decreasing Li_2O content of the mould slag.

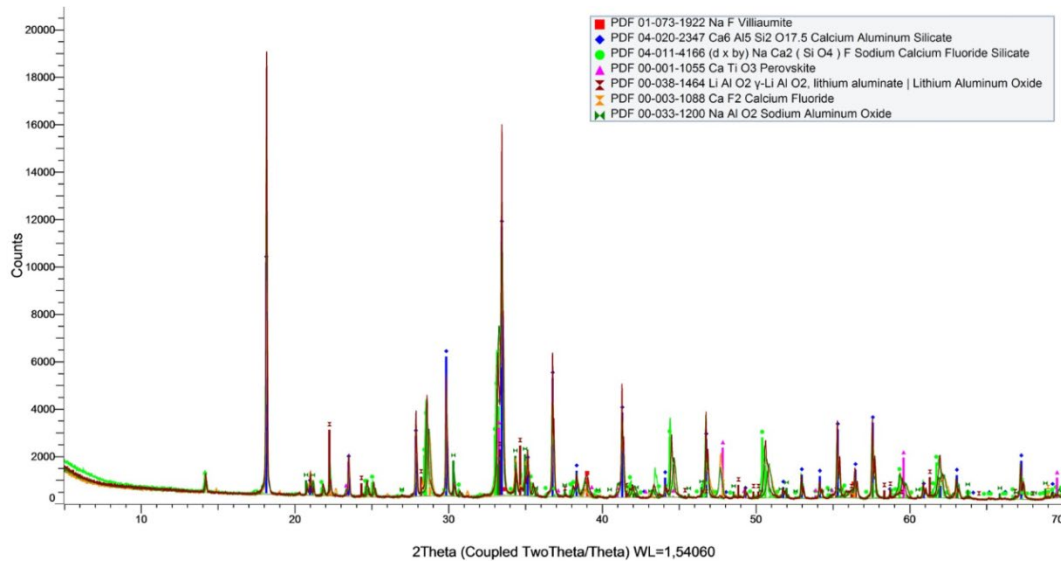


Figure 51: XRD result of sample No.21, No.24, No.25 and 26 with dwell period 15 min

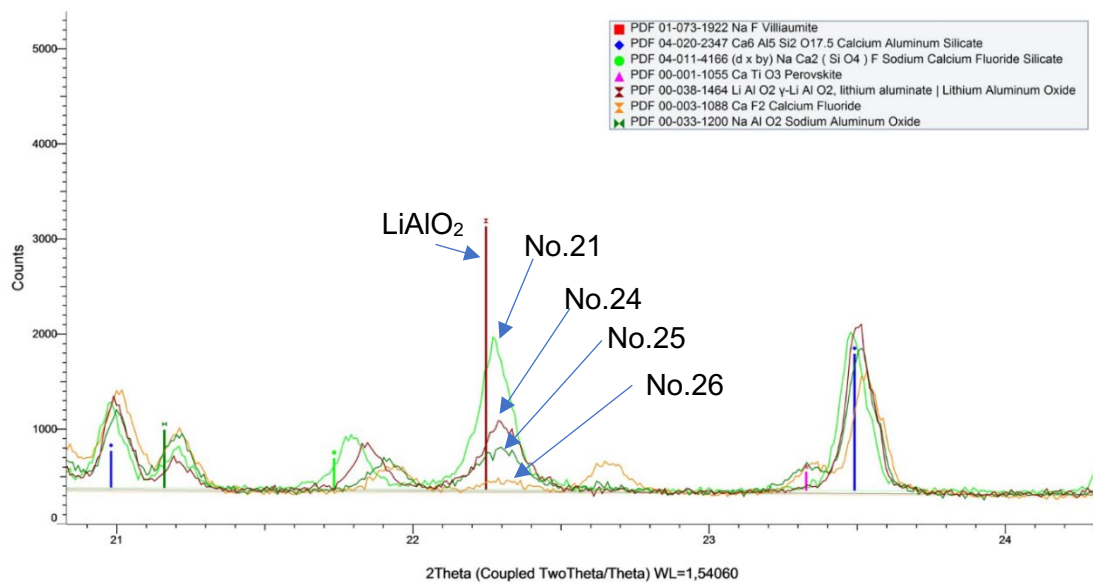


Figure 52: XRD result of LiAlO_2 content change in sample No.21, No.24, No.25 and 26 with dwell period 15 min

As shown in Figure 53, for the same dwell period of 15 min, with varying Li_2O contents, the location of the peaks shift. This is caused by the alteration of other chemical composition in the solid solution of sodium calcium fluoride silicate.

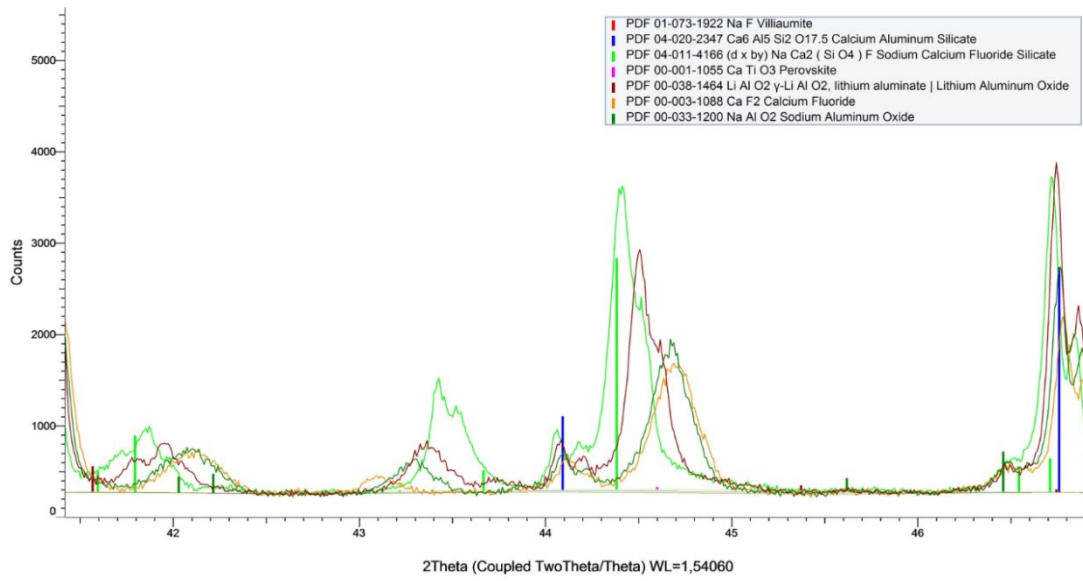


Figure 53: XRD result of Sodium Calcium Fluoride Silicate solid solution in sample No.21, No.24, No.25 and 26 with dwell period 15 min

5 Conclusion

In this thesis, the effect of substitution of SrO and MgO for CaO, and the variation of CaF₂ and Li₂O content on the properties of CaO-Al₂O₃ based mould slag for casting TRIP steel was studied by DTA, XRD, SEM and SHTT. The conclusions are summarized as follows:

1. Substitution of CaO by SrO: Ca²⁺ and Sr²⁺ have the same main coordination number of 8 and similar Dietzal's field strength. This is the reason why Sr²⁺ and Ca²⁺ are interchangeable and can easily form solid solutions. Due to the larger ion radius of Sr²⁺, the viscosity will slightly increase with rising SrO content. The liquidus temperature and the crystallization tendency increase as well.
2. Substitution of CaO by MgO increases the liquidus temperature due to the formation of an additional phase which might be MgO with a high melting point. The crystal fraction increases as well.
3. CaF₂ will work as a network modifier, as long as larger structure units can be broken to single units. Additionally, CaF₂ may act as a network former generating an Al-F-Al bond by dipole – dipole interaction. Therefore, addition of CaF₂ decreases the viscosity only to a certain extent. Due to the overtopping of the platinum crucibles, the viscosity minimum could not be discerned. For the liquidus temperature a minimum was observed at 10.95 mol% CaF₂.
4. Li₂O is the most effective network modifier per weight due to its low molar weight of 30 g/mol. Its small ion radius causes low inner friction in liquidus state. The reduction of lithium oxide leads to the increase of the viscosity, and increase of the Li₂O leads to a significant decrease of the liquidus temperature. Moreover, according to quenching at 900 °C, one of the main phases LiAlO₂ decreases with the decrement of Li₂O content. For constant composition, LiAlO₂ decreases with rising the dwell period.

Up to now, the best result was achieved with composition No. 21 which has a liquidus temperature of 1236 °C and viscosity of 0.283 Pa·s. The liquidus temperature fulfills the requirement. The viscosity is too high, and it may be decreased by increasing the Li₂O content.

Reference

1. Cho, J.-W., K. Blazek, M. Frazee, H. Yin, J.H. Park, and S.-W. Moon, Assessment of CaO–Al₂O₃ based mold flux system for high aluminum TRIP casting. *ISIJ international*, 2013. **53**(1): p. 62-70.
2. Wu, T., Q. Wang, S. He, J. Xu, X. Long, and Y. Lu, Study on Properties of Alumina-Based Mould Fluxes for High-Al Steel Slab Casting. *steel research international*, 2012. **83**(12): p. 1194-1202.
3. Kim, G.H. and I. Sohn, Influence of Li₂O on the viscous behavior of CaO–Al₂O₃–12 mass% Na₂O–12 mass% CaF₂ based slags. *ISIJ international*, 2012. **52**(1): p. 68-73.
4. Fu, X., G. Wen, P. Tang, Q. Liu, and Z. Zhou, Effects of CaO/Al₂O₃ ratio on crystallisation behaviour of CaO–Al₂O₃ based mould fluxes for high aluminium TRIP steel. *Ironmaking & Steelmaking*, 2014. **41**(5): p. 342-341.
5. Yu, X., G. Wen, P. Tang, and H. Wang, Investigation on viscosity of mould fluxes during continuous casting of aluminium containing TRIP steels. *Ironmaking & Steelmaking*, 2009. **36**(8): p. 623-630.
6. Mills, K., A. Fox, Z. Li, and R. Thackray, Performance and properties of mould fluxes. *Ironmaking & steelmaking*, 2005. **32**(1): p. 26-34.
7. Mills, K.C. and A.B. Fox, The role of mould fluxes in continuous casting-so simple yet so complex. *ISIJ international*, 2003. **43**(10): p. 1479-1486.
8. Yoon, D.-W., J.-W. Cho, and S.-H. Kim, Assessment of heat transfer through mold slag film considering radiative absorption behavior of mold fluxes. *Metals and Materials international*, 2015. **21**(3): p. 580-587.
9. Cho, J., H. Shibata, T. Emi, and M. Suzuki, Thermal resistance at the interface between mold flux film and mold for continuous casting of steels. *ISIJ international*, 1998. **38**(5): p. 440-446.
10. Ko, E.-Y., J. Choi, J.-Y. Park, and I. Sohn, Simulation of low carbon steel solidification and mold flux crystallization in continuous casting using a multi-mold simulator. *Metals and Materials International*, 2014. **20**(1): p. 141-151.
11. Park, J.-Y., E.-y. Ko, J. Choi, and I. Sohn, Characteristics of medium carbon steel solidification and mold flux crystallization using the multi-mold simulator. *Metals and Materials International*, 2014. **20**(6): p. 1103-1114.
12. Sahoo, P.P., B.K. Rout, and P. Palai, Mechanism and Control of Hydrogen Induced Abnormal Sticky Behavior in Slab Casting Mould. *ISIJ International*,

2015. **55**(5): p. 993-999.
13. Persson, M., M. Görnerup, and S. Seetharaman, Viscosity measurements of some mould flux slags. *ISIJ international*, 2007. **47**(10): p. 1533-1540.
 14. Zhang, G.-H., K.-C. Chou, and K. Mills, A structurally based viscosity model for oxide melts. *Metallurgical and Materials Transactions B*, 2014. **45**(2): p. 698-706.
 15. Vogel, W., *Glass chemistry*. 2012: Springer Science & Business Media.
 16. Fulcher, G.S., Analysis of recent measurements of the viscosity of glasses. *Journal of the American Ceramic Society*, 1925. **8**(6): p. 339-355.
 17. Shu, Q., Y. Wang, J. Li, Y. Liu, P. Li, and K. Chou, Effect of Na₂O on dissolution rate of alumina in CaO–Al₂O₃–MgO–SiO₂ Slag. *ISIJ International*, 2015. **55**(11): p. 2297-2303.
 18. Zhou, L., W. Wang, D. Huang, J. Wei, and J. Li, In situ observation and investigation of mold flux crystallization by using double hot thermocouple technology. *Metallurgical and Materials Transactions B*, 2012. **43**(4): p. 925-936.
 19. Mills, K.C., Structure and properties of slags used in the continuous casting of steel: Part 2 specialist mould powders. *ISIJ International*, 2016. **56**(1): p. 14-23.
 20. Hooli, P., Study on the layers in the film originating from the casting powder between steel shell and mould and associated phenomena in continuous casting of stainless steel. 2007: Helsinki University of Technology.
 21. Kim, M.-S., S.-W. Lee, J.-W. Cho, M.-S. Park, H.-G. Lee, and Y.-B. Kang, A reaction between high mn-high al steel and CaO-SiO₂-type molten mold flux: part I. Composition evolution in molten mold flux. *Metallurgical and Materials Transactions B*, 2013. **44**(2): p. 299-308.
 22. Wang, H., P. Tang, G. Wen, and X. Yu, Effect of Na₂O on crystallisation behaviour and heat transfer of high Al steel mould fluxes. *Ironmaking & Steelmaking*, 2011. **38**(5): p. 369-373.
 23. Todoroki, H., T. Ishii, K. Mizuno, and A. Hongo, Effect of crystallization behavior of mold flux on slab surface quality of a Ti-bearing Fe–Cr–Ni super alloy cast by means of continuous casting process. *Materials Science and Engineering: A*, 2005. **413**: p. 121-128.
 24. Kanbe, Y., T. Ishii, H. Todoroki, and K. Mizuno, Prevention of longitudinal cracks in a continuously cast slab of Fe–Cr–Ni superalloy containing Al and Ti. *International Journal of Cast Metals Research*, 2009. **22**(1-4): p. 143-146.

25. Zhang, Z., G. Wen, P. Tang, and S. Sridhar, The influence of $\text{Al}_2\text{O}_3/\text{SiO}_2$ ratio on the viscosity of mold fluxes. *ISIJ international*, 2008. **48**(6): p. 739-746.
26. Liu, Q., G. Wen, J. Li, X. Fu, P. Tang, and W. Li, Development of mould fluxes based on lime–alumina slag system for casting high aluminium TRIP steel. *Ironmaking & Steelmaking*, 2014. **41**(4): p. 292-297.
27. Neuville, D., L. Cormier, V. Montouillout, and D. Massiot, Local Al site distribution in aluminosilicate glasses by ^{27}Al MQMAS NMR. *Journal of Non-Crystalline Solids*, 2007. **353**(2): p. 180-184.
28. Li, J., Q. Shu, X. Hou, and K. Chou, Effect of TiO_2 Addition on Crystallization Characteristics of $\text{CaO-Al}_2\text{O}_3$ -based Mould Fluxes for High Al Steel Casting. *ISIJ International*, 2015. **55**(4): p. 830-836.
29. Gao, E., W. Wang, and L. Zhang, Effect of alkaline earth metal oxides on the viscosity and structure of the $\text{CaO-Al}_2\text{O}_3$ based mold flux for casting high-al steels. *Journal of Non-Crystalline Solids*, 2017. **473**: p. 79-86.
30. Levin, E.M., Phase diagrams for ceramics. *The Am. Ceram. Soc.*, 1964. **11**: p. 219-219.
31. Kim, H. and I. Sohn, Effect of CaF_2 and Li_2O additives on the viscosity of $\text{CaO-SiO}_2\text{-Na}_2\text{O}$ slags. *ISIJ international*, 2011. **51**(1): p. 1-8.
32. Liu, H., G. Wen, and P. Tang, Crystallization behaviors of mold fluxes containing Li_2O using single hot thermocouple technique. *ISIJ international*, 2009. **49**(6): p. 843-850.
33. Lu, B., K. Chen, W. Wang, and B. Jiang, Effects of Li_2O and Na_2O on the crystallization behavior of lime-alumina-based mold flux for casting high-Al steels. *Metallurgical and Materials Transactions B*, 2014. **45**(4): p. 1496-1509.
34. Tsunawaki, Y., N. Iwamoto, T. Hattori, and A. Mitsuishi, Analysis of CaO-SiO_2 and $\text{CaO-SiO}_2\text{-CaF}_2$ glasses by Raman spectroscopy. *Journal of Non-Crystalline Solids*, 1981. **44**(2-3): p. 369-378.
35. Gao, Q., Y. Min, C.-j. Liu, and M.-f. Jiang, Structural behavior of F⁻ in mould flux melt of $\text{CaO-SiO}_2\text{-Al}_2\text{O}_3\text{-Na}_2\text{O-CaF}_2$ system. *Journal of Iron and Steel Research, International*, 2017. **24**(11): p. 1152-1158.
36. Klug, J.L., D.R. Silva, S.L. Freitas, M.M. Pereira, N.C. Heck, A.C. Vilela, and D. Jung, Fluorine - Free Mould Powders for Billet Casting – Technological Parameters and Industrial Tests. *Steel research international*, 2012. **83**(8): p. 791-799.
37. Higo, T., S. Sukenaga, K. Kanehashi, H. Shibata, T. Osugi, N. Saito, and K.

- Nakashima, Effect of potassium oxide addition on viscosity of calcium aluminosilicate melts at 1673–1873 K. *ISIJ International*, 2014. **54**(9): p. 2039-2044.
38. Bale, C.W., E. Bélisle, P. Chartrand, S. Deckerov, G. Eriksson, A. Gheribi, K. Hack, I.-H. Jung, Y.-B. Kang, and J. Melançon, FactSage thermochemical software and databases, 2010–2016. *Calphad*, 2016. **54**: p. 35-53.
39. NETZSCH LLC, STA 449 F3 Jupiter®. Home page: <https://www.netzsch-thermal-analysis.com/en/products-solutions/simultaneous-thermogravimetry-differential-scanning-calorimetry/sta-449-f3-jupiter/> (02.05.2019)
40. Kromhout, J., A. Kamperman, M. Kick, and J. Trouw, Mould powder selection for thin slab casting. *Ironmaking & steelmaking*, 2005. **32**(2): p. 127-132.
41. Goldstein, J.I., D.E. Newbury, J.R. Michael, N.W. Ritchie, J.H.J. Scott, and D.C. Joy, *Scanning electron microscopy and X-ray microanalysis*. 2017: Springer.
42. Kacher, J., C. Landon, B.L. Adams, and D. Fullwood, Bragg's Law diffraction simulations for electron backscatter diffraction analysis. *Ultramicroscopy*, 2009. **109**(9): p. 1148-1156.
43. Dey, A. and S. Riaz, Viscosity measurement of mould fluxes using inclined plane test and development of mathematical model. *Ironmaking & Steelmaking*, 2012. **39**(6): p. 391-397.

Appendix

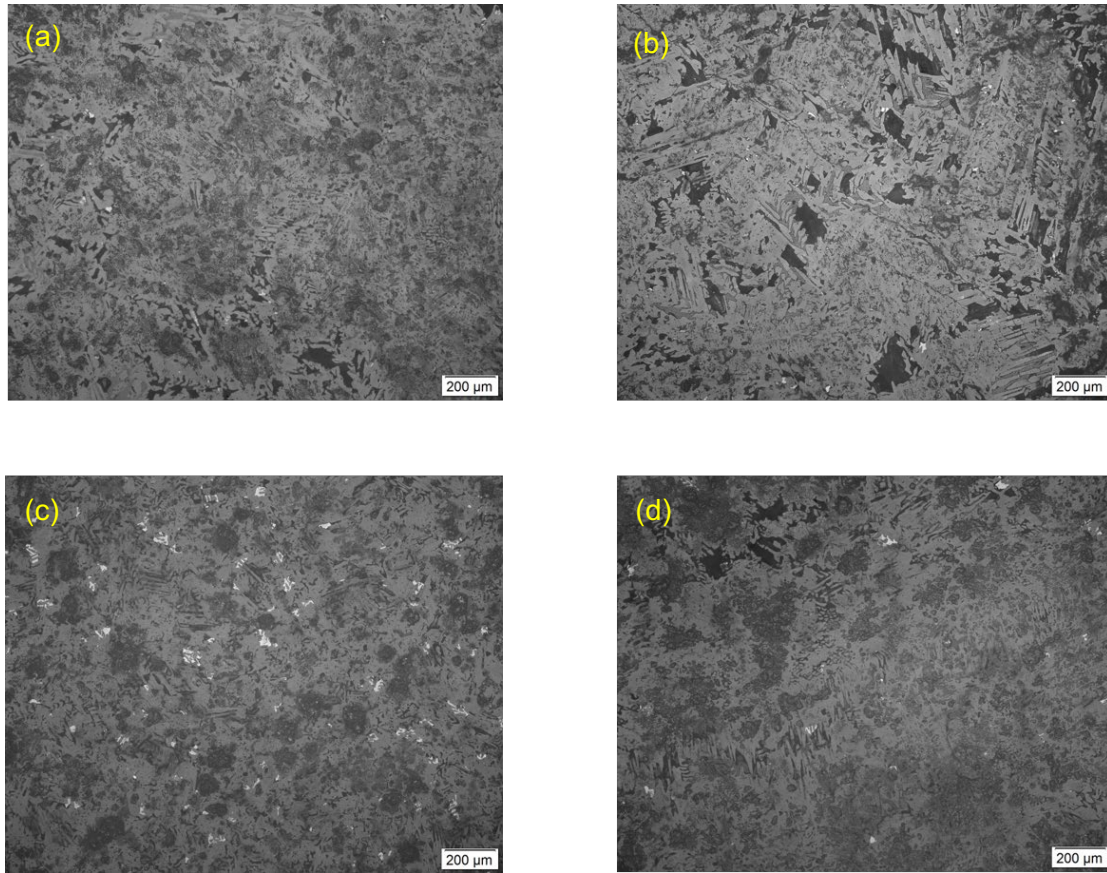


Figure A-1: Optical microscope pictures; a) of sample No.24 dwell 5 min; b) of sample No.24 dwell 15 min; c) of sample No.24 dwell 30 min; d) of sample No.24 dwell 60 min; The crystal size increases with increasing dwell period.

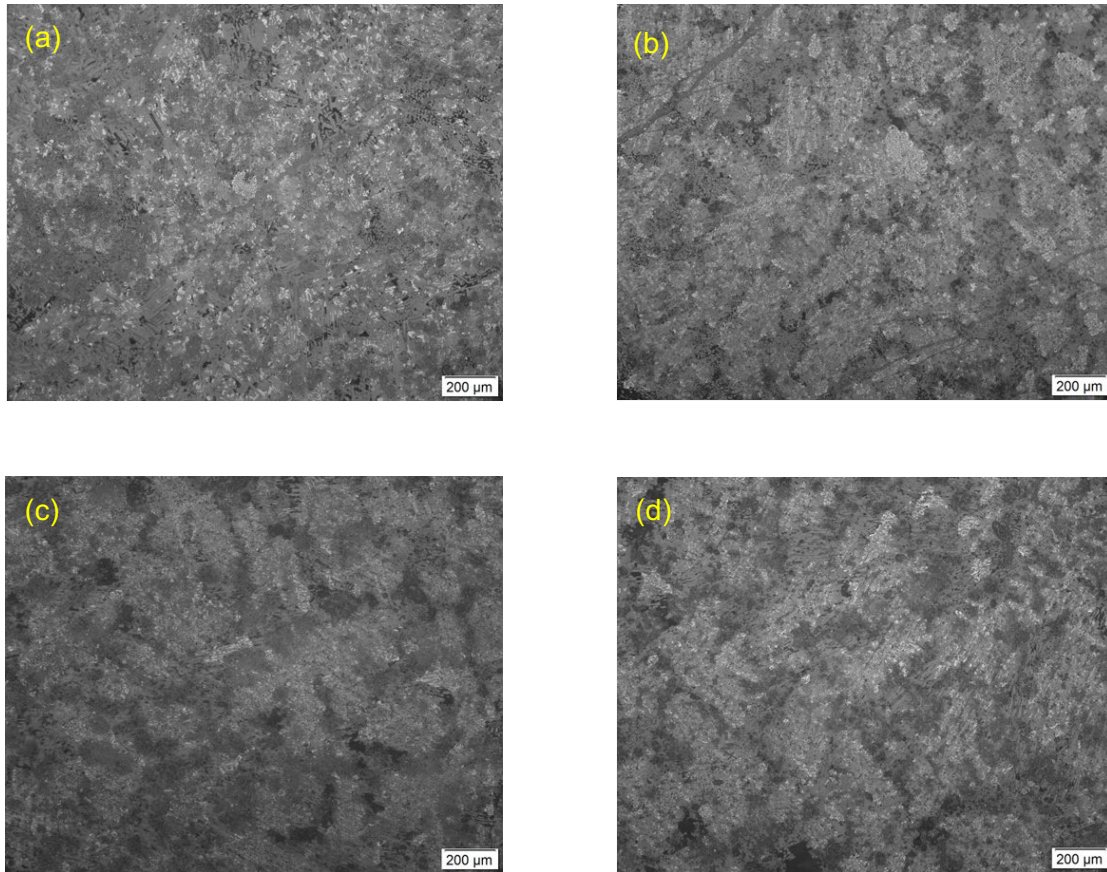


Figure A-2: Optical microscope pictures; a) of sample No.25 dwell 5 min; b) of sample No.25 dwell 15 min; c) of sample No.25 dwell 30 min; d) of sample No.25 dwell 60 min; The crystal size increases with increasing dwell period.

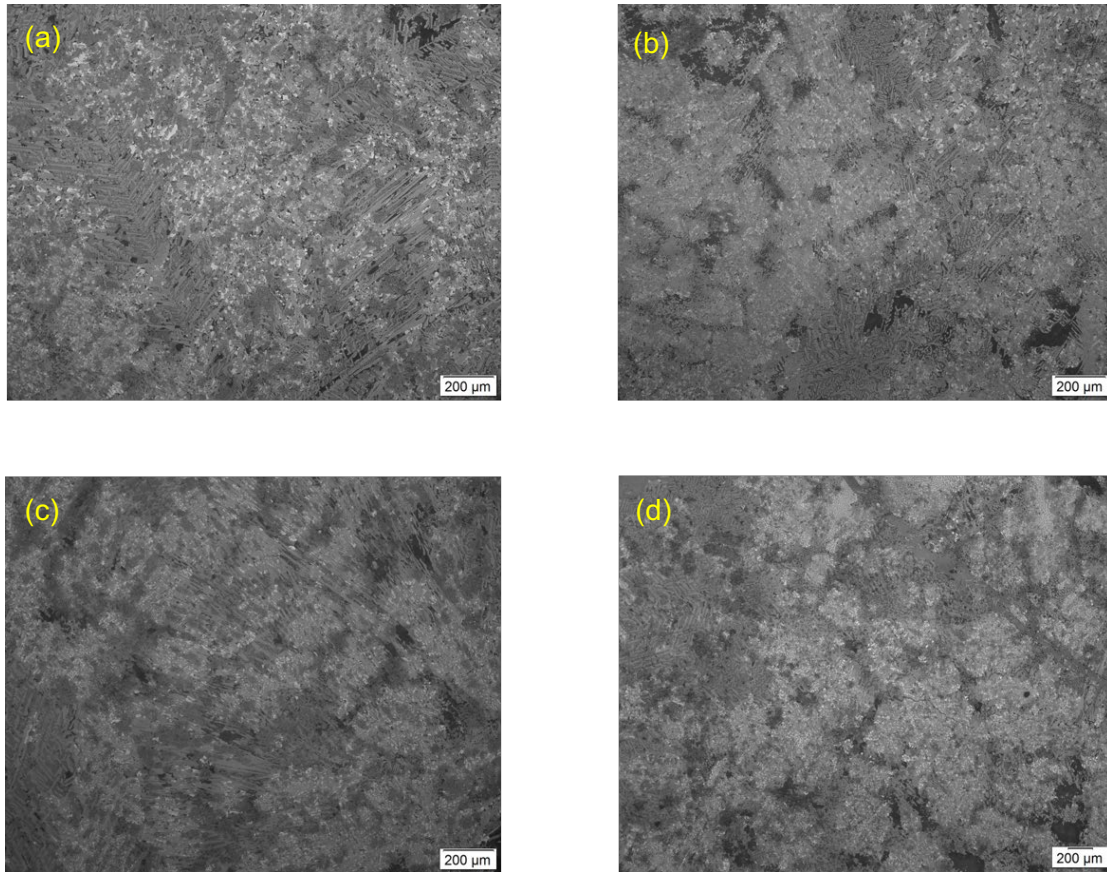


Figure A-3: Optical microscope pictures; a) of sample No.26 dwell 5 min; b) of sample No.26 dwell 15 min; c) of sample No.26 dwell 30 min; d) of sample No.26 dwell 60 min; The crystal size increases with increasing dwell period.

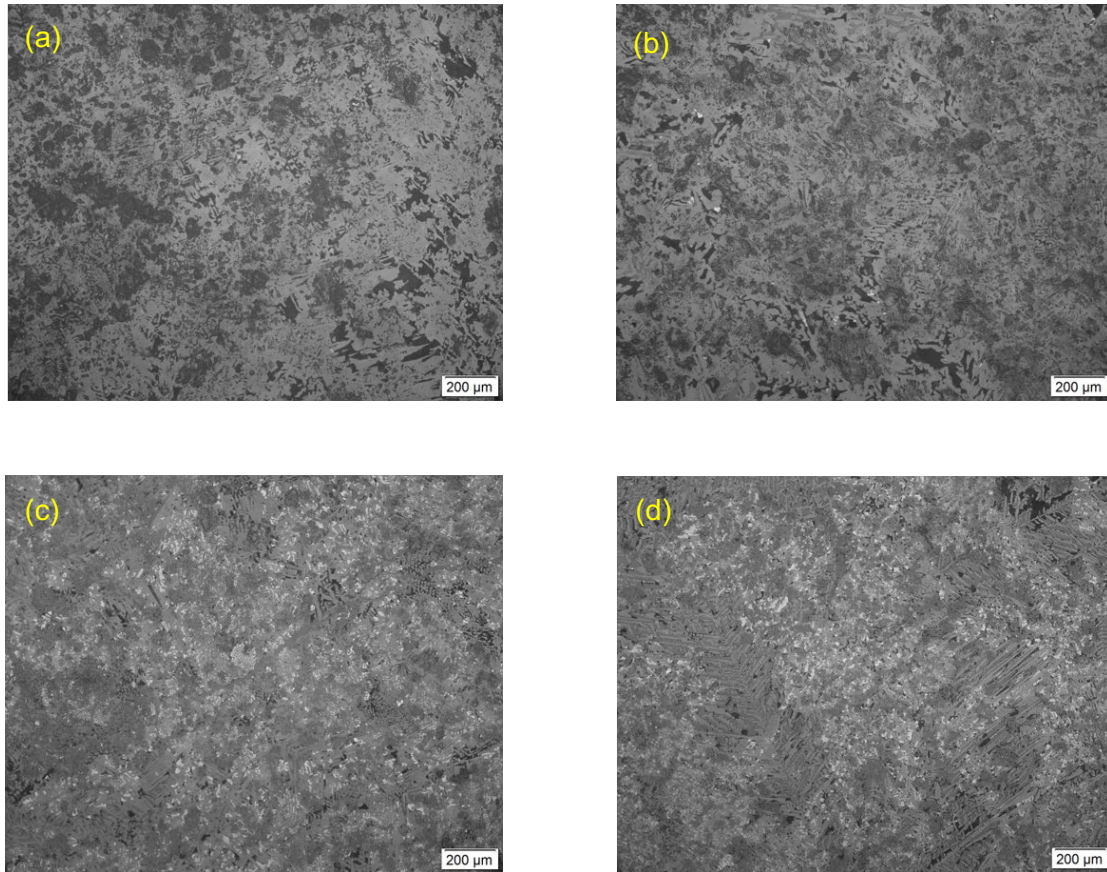


Figure A-4: Optical microscope pictures; a) of sample No.21 dwell 5 min; b) of sample No.24 dwell 5 min; c) of sample No.25 dwell 5 min; d) of sample No.26 dwell 5 min; The crystal size decreases with decreasing Li_2O content.

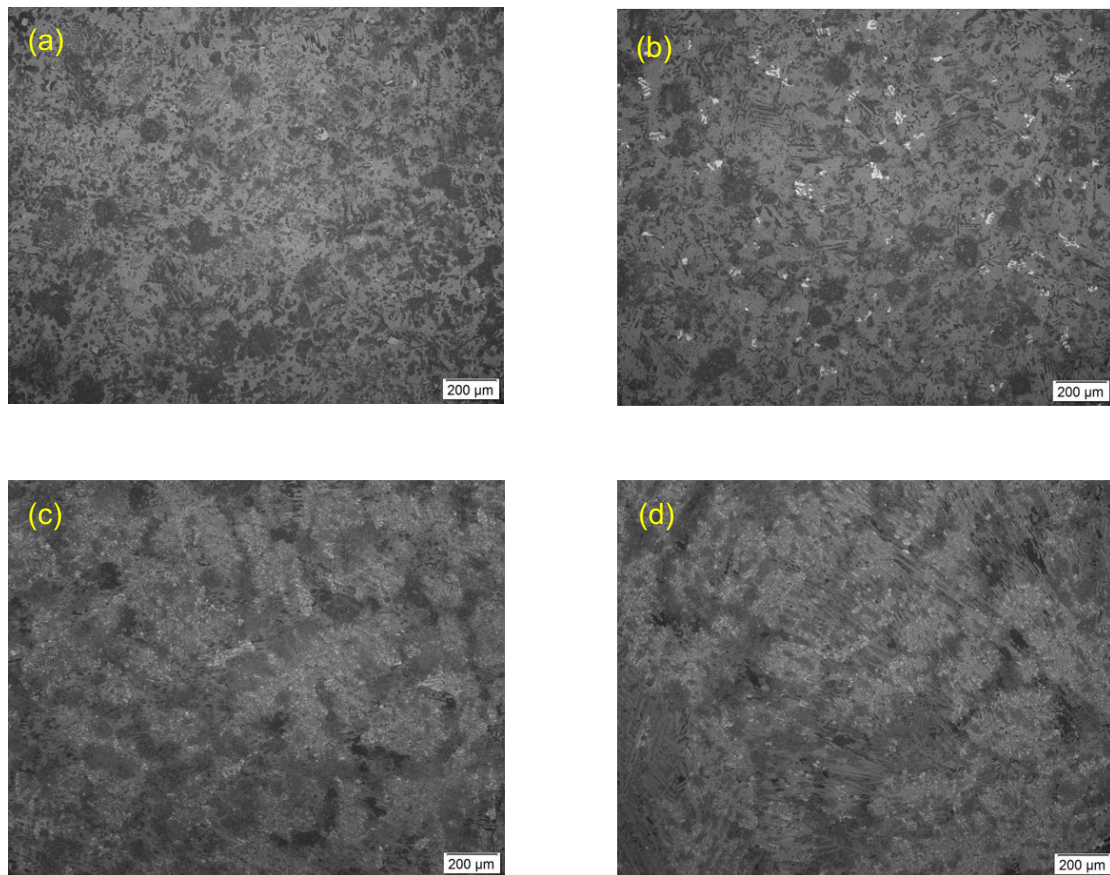


Figure A-5: Optical microscope pictures; a) of sample No.21 dwell 30 min; b) of sample No.24 dwell 30 min; c) of sample No.25 dwell 30 min; d) of sample No.26 dwell 30 min; Crystal size decreases with decreasing Li_2O content.

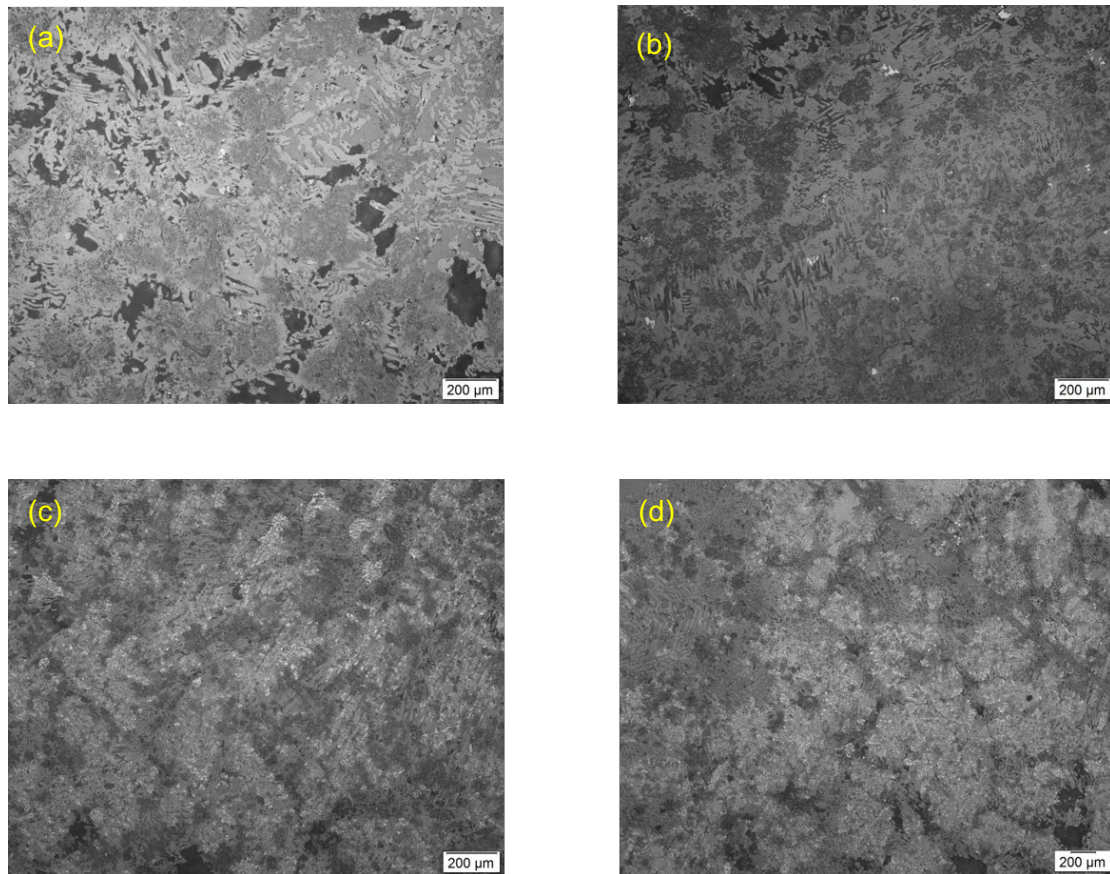


Figure A-6: Optical microscope pictures; a) of sample No.21 dwell 60 min; b) of sample No.24 dwell 60 min; c) of sample No.25 dwell 60 min; d) of sample No.26 dwell 60 min; Crystal size decreases with decreasing Li_2O content.

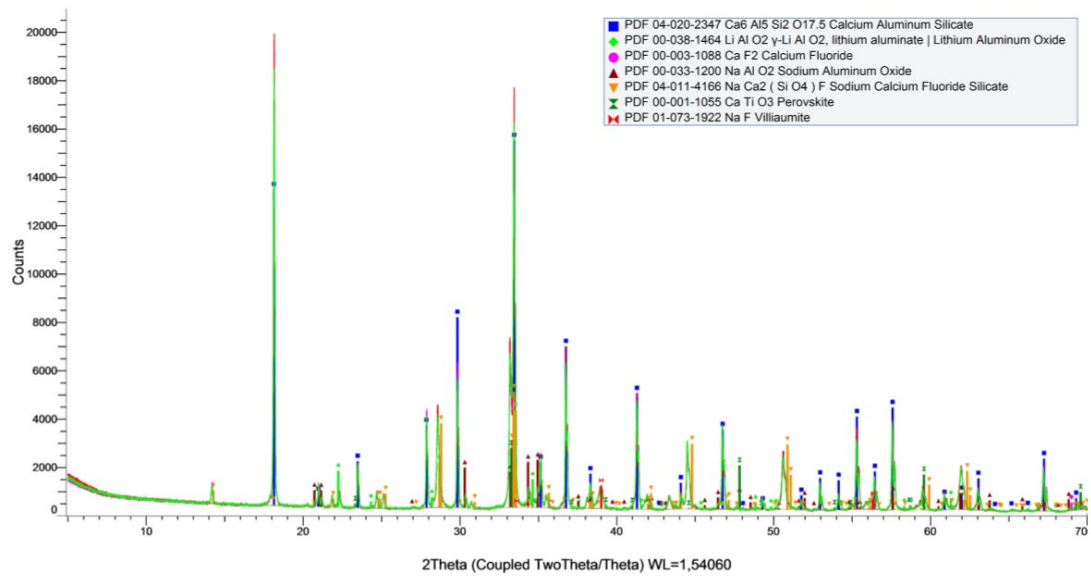


Figure A-7: XRD result of sample No.24 with dwell period 5 min, 15 min, 30 min and 60 min

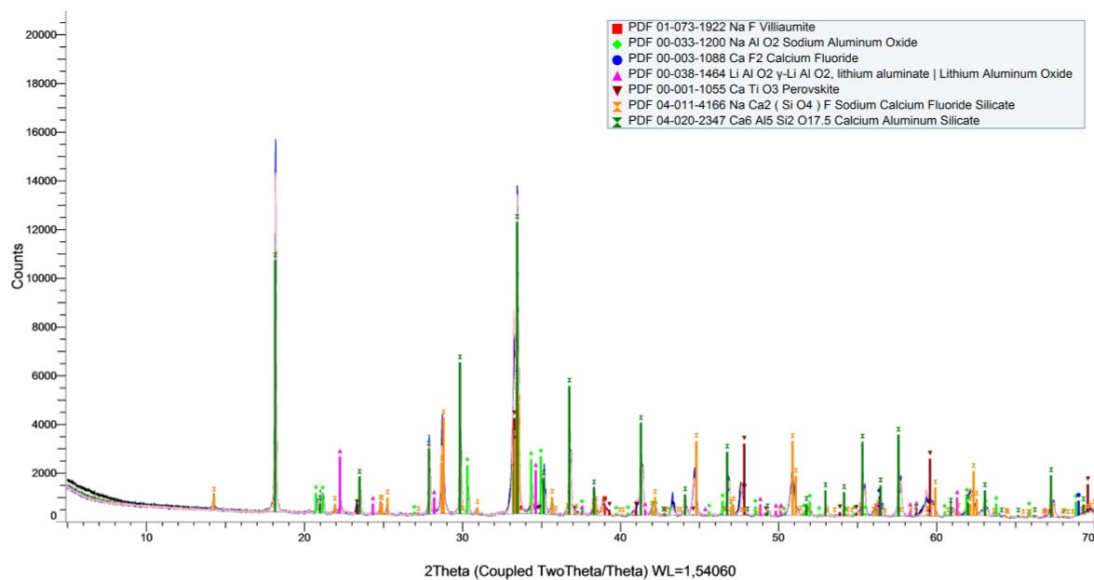


Figure A-8: XRD result of sample No.25 with dwell period 5 min, 15 min, 30 min and 60 min

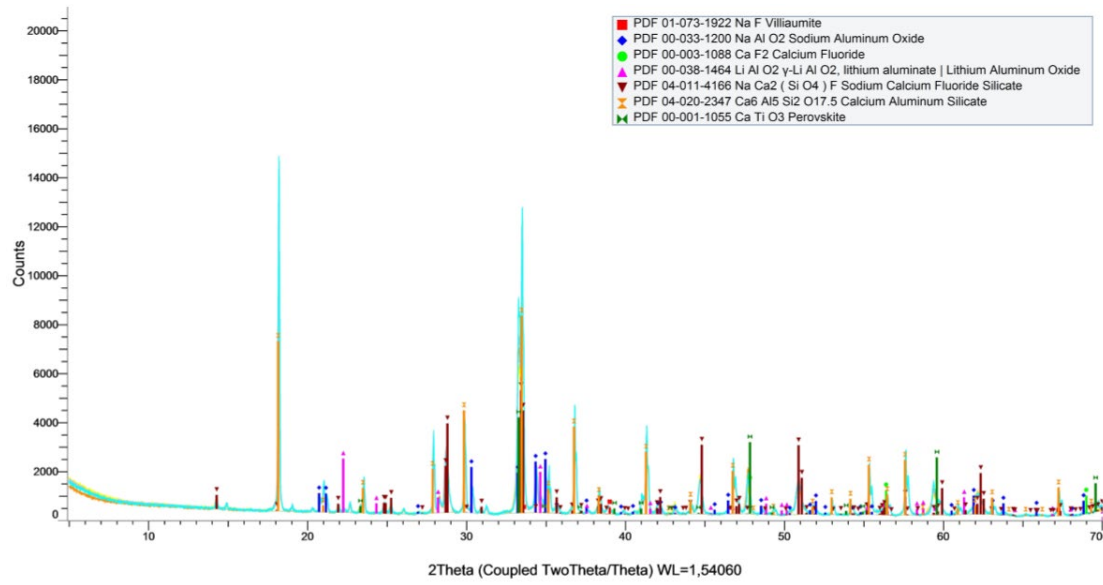


Figure A-9: XRD result of sample No.26 with dwell period 5 min, 15 min, 30 min and 60 min